Bergische Universität Wuppertal
Fakultät für
Mathematik und Naturwissenschaften
Fachgruppe Physik

Search for high-mass dilepton resonances in association with b-jets at the ATLAS experiment

Thesis
zur Erlangung des akademischen Grades
Master of Science (M.Sc.)
im Studiengang Physik
der Bergischen Universität Wuppertal

vorgelegt von Maren Stratmann

Erstgutachter: Priv. Doz. Dr. Frank Ellinghaus
Zweitgutachter: Prof. Dr. Wolfgang Wagner
Abgabedatum: 4. November 2021

Abstract

In this thesis, a search for a Z' boson produced in association with b-jets is presented. The analysis uses the data from proton-proton collisions at a centre-of-mass energy of $\sqrt{s} = 13\,\text{TeV}$ collected by the ATLAS detector in 2015 and 2016, corresponding to an integrated luminosity of $36.2\,\text{fb}^{-1}$. A preliminary expected limit on the Z' production cross section is set to compare the sensitivity of the analysis approach to the sensitivity of previous inclusive searches. Systematic uncertainties are not considered.
The analysis is carried out separately in the electron channel and the muon channel. A preselection region is defined, and the most important background processes are validated in dedicated regions. For the electron channel, a data-driven estimation of the multijet background is obtained via the Matrix Method. The Monte Carlo samples of the signal process are studied, and two different approaches for defining a signal region are introduced. A preliminary limit on the Z' production cross section is set and compared to the limit obtained by previous inclusive analyses. The limit on the Z' mass obtained in this analysis is lower than the limit obtained by the inclusive analyses. Overall, the chosen analysis approach is found to be limited by low event statistics in the high dilepton invariant mass region. The expected limits on the production cross section are lower than the limits of the inclusive analysis, but the smaller production cross section results in a lower exclusion limit on the Z' mass as well.

Contents

1. Introduction

The Standard Model of particle physics (SM) is a theory developed in the second half of the 20th century to describe the properties of elementary particles and their interactions. Although the SM provides a successful description for most observations, some phenomena such as the non-zero neutrino mass or anomalies measured in rare decay processes of b quarks give room for Beyond Standard Model (BSM) theories. One such extension of the SM is the prediction of a new heavy gauge boson, the so-called Z', aiming to explain the deviations from the SM prediction observed in rare b quark decays by mediating the $b \to s$ quark transition at leading order. The Z' considered in this thesis couples predominantly to quarks of the third generation, electrons and muons. The coupling to quarks of the second generation is suppressed by the CKM matrix and a coupling to first generation quarks is forbidden.

Collision experiments provide an opportunity to study the properties of elementary particles and their interactions. The largest particle collider is the Large Hadron Collider (LHC) at CERN with a circumference of 27 km. Several experiments are performing measurements of the collisions at the LHC, one of which is the ATLAS (A Toroidal LHC ApparatuS) experiment.
The analysis presented in this thesis uses the data collected by the ATLAS detector in 2015 and 2016, corresponding to an integrated luminosity of $36.2\,\mathrm{fb}^{-1}$. A search for a Z' produced in association with b-jets is performed, with the Z' decaying leptonically. Previous searches for a Z' in the dilepton channel have been performed using an inclusive Z' production. The aim of this thesis is to study whether the search for a Z' produced in association with b-jets achieves a higher sensitivity than the previous searches for an inclusive production.

This thesis is structured as follows: Chapter 2 provides a short introduction to the SM as well as the motivation for and theoretical background of the considered Z' model. The LHC and the ATLAS experiment are introduced in Chapter 3. A description of the datasets and simulated samples used for the analysis is given in Chapter 4, followed by the definitions of objects reconstructed from the detector information in Chapter 5. In Chapter 6, the event selection criteria used as a starting point for the analysis are presented as well as the data-driven estimation of the so-called multijet background and the validation of the agreement between data and simulated samples. A study of the simulated samples of the signal process is presented in Chapter 7 together with two different approaches of defining a signal region. The procedure of setting a limit on the signal strength, as well as a comparison of the obtained limits with a previous inclusive analysis, is presented in Chapter 8. A conclusion of the results and an outlook on further analysis steps is given in Chapter 9.

2. Theory

This chapter provides an overview of the theoretical background of the analysis presented in this thesis. The SM is described in Section 2.1, followed by the motivation for the search of a new boson as well as the theoretical model of the considered boson in Section 2.2. Section 2.3 provides information on the physics of proton-proton collisions.

2.1. The Standard Model of Particle Physics

The SM is a quantum field theory describing the elementary particles and their interactions via the strong, weak and electromagnetic force [1]. It was developed in the 1960s and 1970s and has proven to be successful in predicting the existence of particles and their properties, with the latest discovered particle being the Higgs boson found in 2012 [2, 3].
An overview of the elementary particles is given in Figure 2.1. The particles are grouped into fermions with half-integer spin and bosons with integer spin. Fermions are further divided into quarks and leptons, consisting of six particles each. Quarks are sorted into up- and down-type quarks according to their electrical charge and grouped into three generations, consisting of the flavours up and down, charm and strange, top and bottom respectively. Quarks carry colour charge and can therefore interact via the strong interaction, as distinguished from leptons.

Leptons are further divided into electrically charged leptons and neutrinos, which carry no electrical charge. The three lepton generations consist of electron, muon, tauon and a neutrino with associated flavour. Of the charged leptons, only electrons are stable as they have the lowest mass.
Bosons are the mediators of the fundamental forces. Gluons are massless bosons existing in eight different colour-eigenstates, mediating the strong force acting on the colour charge of quarks. As the strength of the strong coupling increases linearly with the distance, quarks cannot be observed as free particles, but only in bound states with zero net colour charge. Particles consisting of quarks are called hadrons and further divided into baryons consisting of three quarks and mesons consisting of a quark-antiquark pair.
The second type of massless bosons are photons, mediating electromagnetic interactions between electrically charged particles. The neutral Z boson and the two electrically charged $W^{\pm}$ bosons are the exchange particles of the weak force, being the only force to act on all fermions. The $W^{\pm}$ bosons are the only bosons mediating flavour-changing currents between quarks, with the transition probability between the different quark flavours being described by the CKM matrix [5]. The matrix is almost diagonal, meaning that flavour changes mostly occur between quarks of the same generation. The Higgs boson is the only known elementary particle with zero spin and mediates the coupling of elementary particles to the Higgs field, with the strength of the coupling determining the masses of particles.

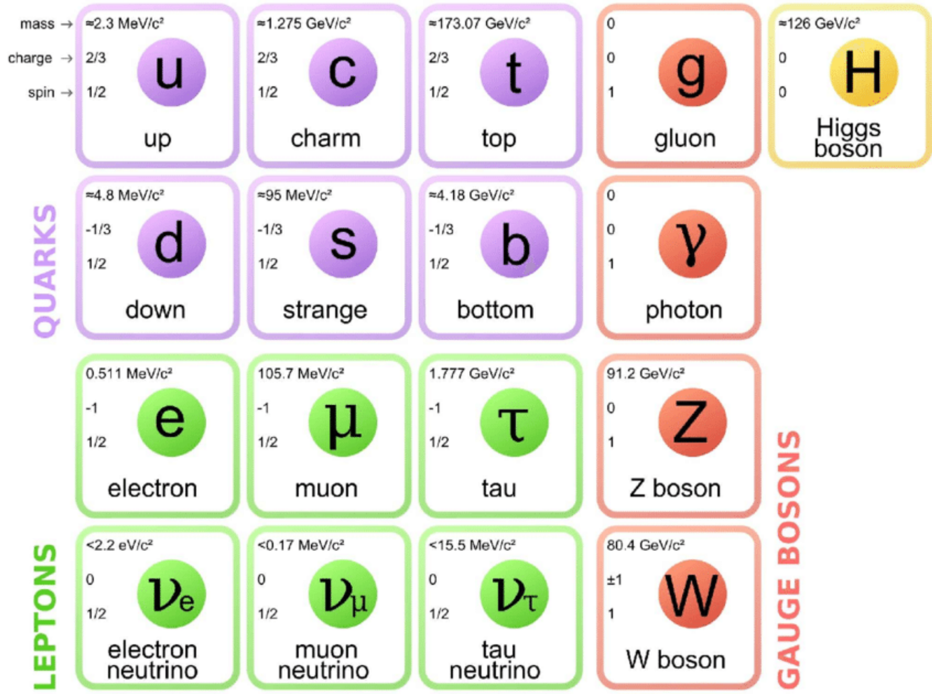

Figure 2.1.: Particles of the Standard Model of particle physics [4].

The gravitational force not being included in the SM is one of the motivations for BSM theories. A variety of these theories exists, aiming to explain measurements exhibiting deviations from the SM predictions, some of which are discussed in Section 2.2.1, and other phenomena not covered by the SM, such as the non-zero neutrino mass or the existence of dark matter.

2.2. New heavy gauge boson

One candidate for an extension of the SM is a new heavy vector boson, the so-called Z' [6]. It offers an explanation for deviations from SM predictions observed in decay processes involving a $b \to s$ quark transition. An overview of the observed deviations is given in Section 2.2.1, and the Z' model studied in this analysis is presented in Section 2.2.2.

2.2.1. B-quark decay anomalies

In the SM, flavour-changing neutral currents (FCNCs), such as processes involving a $b \to s$ transition, are forbidden at leading order and therefore not mediated by the Z boson. At next-to-leading order, FCNCs are allowed but suppressed by the GIM-mechanism [7]. Therefore, these so-called rare b-decay processes are studied in the search for BSM physics, as they are sensitive to the contribution of new particles.
The process of a B-meson decaying into a Kaon B→ K$\ell^+\ell^-$, corresponding to the quark

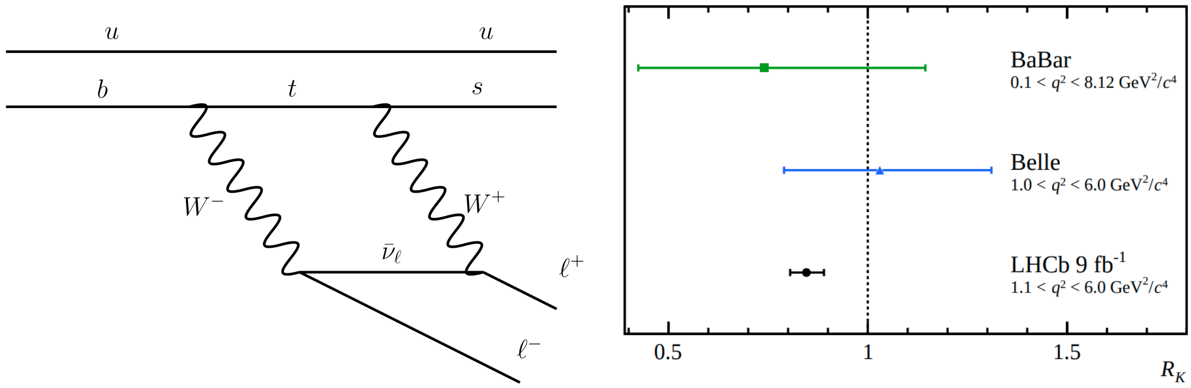

Figure 2.2.: SM $B^+ \to K^+\ell^+\ell^-$ decay process (left) and measurement result of the R_K ratio [8] (right).

transition $b \to s\ell^+\ell^-$, exhibits deviations from SM predictions in the branching ratios [8] as well as in angular distributions [9]. The ratio of the branching ratios for final states including electrons and muons $R_K = \frac{B^+\to K^+\mu^+\mu^-}{B^+\to K^+e^+e^-}$ has been found to differ from one for low values of the squared dilepton invariant mass, hinting at lepton-flavour universality violation. The latest and most precise measurement of R_K, which is presented in Figure 2.2 together with the SM process mediating the decay, observed a deviation of 3.1σ from the SM prediction. For the measurement of angular distributions, special observables are constructed to be independent of theoretical uncertainties in the modelling of the $b \to s$ transition [10]. One of these observables, called P_5', is presented in Figure 2.3. It exhibits a persistent deviation from the SM prediction of 2.6σ, hinting at the existence of an additional boson mediating the $b \to s$ decay at leading order. Global fits taking all observables of rare b-decays into account have found models with BSM contribution to agree better than the SM prediction by more than 5σ, providing strong evidence for BSM physics in rare b-decays [11].

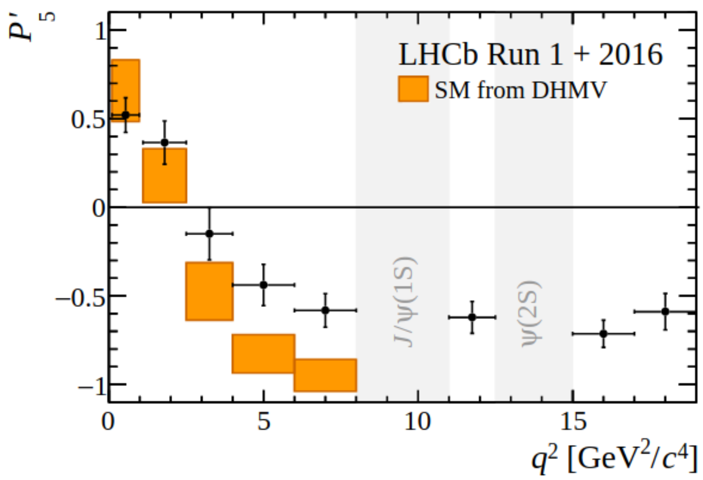

Figure 2.3.: Measurement result of the P_5' observable [9].

2.2.2. The Z' model

The Z' model studied in this analysis was initially proposed to explain the discrepancy in the angular distributions of $B \rightarrow K^{*}\mu^{+}\mu^{-}$ decays [6]. The Z' is a new heavy vector boson carrying no electrical charge and mediating the decay $b \rightarrow s$ at leading order, with the coupling of the Z' to s quarks being suppressed by the CKM matrix element $|V_{cb}|$. Couplings to first-generation quarks are forbidden, as the resulting cross section predictions for the Z' production are experimentally excluded.
The Z' model only allows couplings to left-handed fermions, introducing the left-handed chirality operator P_L to the lagrangian:

$$\begin{aligned}\mathcal{L}_{LH} = {} & g_{Z'b}\bar{b}\gamma^{\nu}P_L b Z'_{\nu} + g_{Z'\ell}\bar{\ell}\gamma^{\nu}P_L \ell Z'_{\nu} + g_{Z't}\bar{t}\gamma^{\nu}P_L t Z'_{\nu} \\ & + g_{Z's}\bar{s}\gamma^{\nu}P_L s Z'_{\nu} + g_{Z'bs}\bar{b}\gamma^{\nu}P_L s Z'_{\nu} + g_{Z'bs}\bar{s}\gamma^{\nu}P_L b Z'_{\nu},\end{aligned} \tag{2.1}$$

with the ℓ representing either electron or muon, $\ell = e/\mu$, and the couplings $g_{Z'x}$ fulfilling the relations

$$\begin{aligned} g_{Z'b} &= g_{Z't} = g_{Z'\ell} \\ g_{Z'bs} &= |V_{cb}| \cdot g_{Z'b} \\ g_{Z's} &= |V_{cb}|^2 \cdot g_{Z'b}. \end{aligned}$$

Two interactions that are considered as possible signal processes for this analysis are presented in Figure 2.4. The final state of the signal processes is characterized by the presence of two leptons of opposite electrical charge and same flavour in combination with at least one b-jet. The existence of a Z' coupling only to muons would account for both deviations from SM predictions presented in Section 2.2.1. As other BSM models include new physics contributions retaining lepton flavour universality [11], signal processes involving a Z'$\rightarrow ee$ decay are also considered.

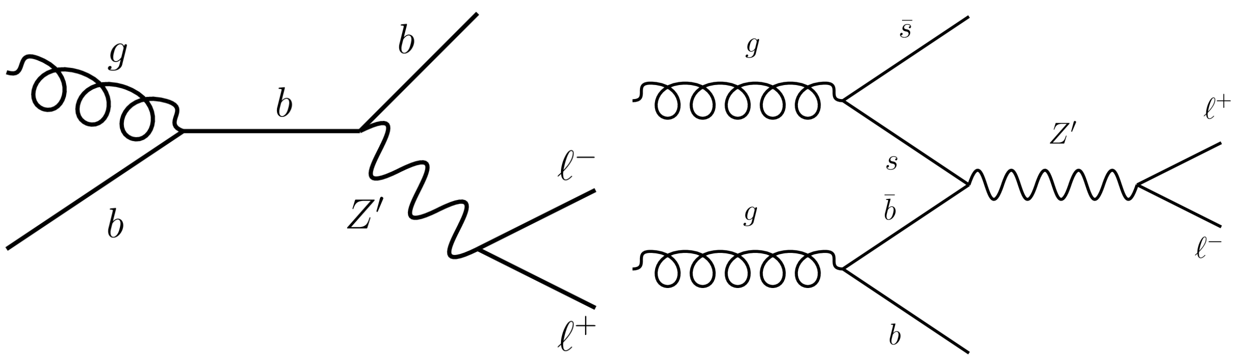

Figure 2.4.: Possible signal processes with a Z' being radiated off a b quark (left) and a Z' mediating a leading order coupling between a b- and s-quark (right).

2.3. Proton collision physics

Proton-proton collisions at high centre-of-mass energies result in interactions at parton level which are split into different stages to allow for a mathematical description and modelling of the whole process. The initial interaction of two partons is referred to as hard scattering process. It takes place at high energies and can be calculated in perturbation theory. The quarks and gluons present in the final state of the interaction produce additional particles via gluon radiation and gluons splitting into quark-antiquark pairs, decreasing the energy of the particles in the parton shower until hadrons are formed. This hadronization is a non-perturbative process as it takes place at low energies, requiring different modelling techniques than the hard scattering process [12].
The proton substructure is modelled with Parton Distribution Functions (PDFs) which describe the probability for a parton i to carry the fraction x_i of the total proton momentum when probed at the energy scale μ^2. The PDFs are used to calculate the cross sections for the hard scattering processes. Two examples for proton PDFs at different energy scales are presented in Figure 2.5. It can be seen how the three valence quarks carry most of the momentum, but the contribution of the sea-quarks and gluons increases with the energy scale, increasing the probability for those partons to take part in an interaction.

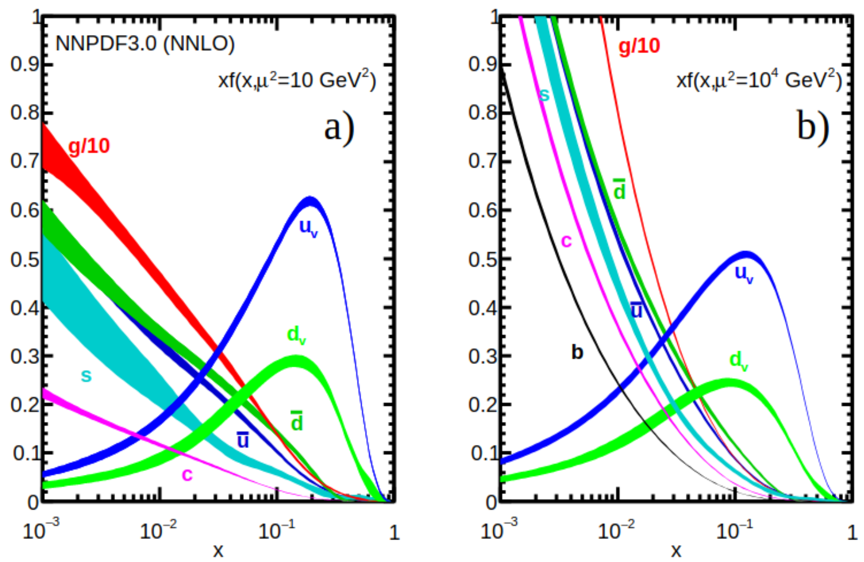

Figure 2.5.: Proton PDF calculated with NNPDF3.0 [13] for an energy scale $\mu^2 = 10\,\text{GeV}^2$ (left) and $\mu^2 = 10^4\,\text{GeV}^2$ (right) [14].

3. The ATLAS Detector at the LHC

Collision experiments are used in high-energy particle physics to study the interactions of elementary particles, and thereby measure their properties and probe the SM as well as theories for BSM physics. The analysis presented in this thesis uses data collected by the ATLAS detector at the LHC. Therefore, the collider and the detector are introduced in the following chapter. Section 3.1 gives an overview of the LHC, and Section 3.2 describes the ATLAS detector and its components.

3.1. The Large Hardon Collider

The LHC at CERN near Geneva is a particle accelerator and collider with a circumference of 27 km, making it the largest particle accelerator worldwide [15]. It is designed for proton-proton and heavy-ion collision experiments and was installed in the tunnel originally build for the Large Electron Positron collider (LEP), which operated until 2000.

Figure 3.1 gives an overview of the accelerator complex at CERN. The acceleration chain starts with the linear accelerator Linac 2, where hydrogen atoms are stripped of their electrons in order to produce protons which are then accelerated to an energy of 50 MeV. In 2018, Linac 2 was replaced by its successor Linac 4 which accelerates the protons to an energy of 160 MeV. The protons are then further accelerated by the Proton Synchrotron Booster, the Proton Synchrotron and the Super Proton Synchrotron from where the protons are finally injected into the beam pipes of the LHC with an energy of 450 GeV.
The LHC consists of two beam pipes, as the counter-rotating proton beams needed for collision experiments cannot share a single beam pipe. The beam pipes are not filled continuously, but the protons travel in bunches consisting of up to $1.25{\cdot}10^{11}$ protons each with a distance of 25 ns in between, which corresponds to a collision frequency of 40 MHz. The proton bunches are kept on track by superconducting dipole magnets, which generate magnetic fields of up to 8 T, and are brought to collision at four designated collision points at which the main detectors of the LHC are positioned.
ATLAS [17] and CMS (Compact Muon Solenoid) [18] are general-purpose detectors designed to enable a variety of measurements, ranging from QCD precision tests to BSM physics. The LHCb [19] detector is a forward-spectrometer dedicated to studying heavy-flavour physics and rare b-decays in particular. ALICE (A Large Ion Collider Experiment) [20] is a detector dedicated to heavy-ion physics, aiming to study QCD interactions at high energy densities in Pb-Pb collisions.
The LHC started to operate in 2010 with proton-proton collisions reaching a centre-of-mass energy of $\sqrt{s} = 7\,\text{TeV}$ which increased to $\sqrt{s} = 8\,\text{TeV}$ towards the end of the first data-taking period, the so-called Run 1, in 2012. After the first long shutdown in 2013 and 2014, operation continued with the second data-taking period, called Run 2, and lasted from 2015 to 2018 with a collision energy of $\sqrt{s} = 13\,\text{TeV}$. The second long shutdown concluded in

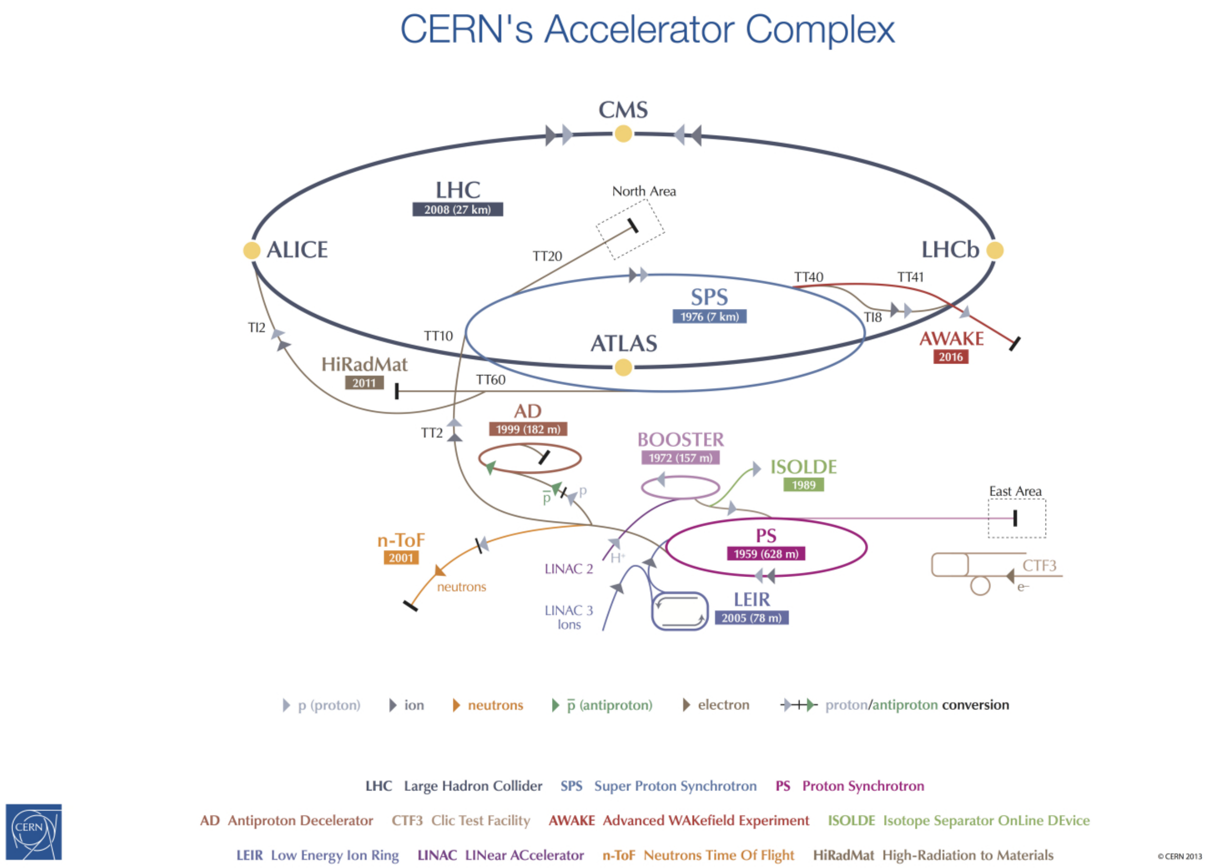

Figure 3.1.: Schematic representation of CERN's acceleration complex [16].

2021, followed by a phase of hardware commissioning and magnet training [21]. The third data-taking period, called Run 3, is scheduled to start in 2022.
Another important characteristic of a particle collider besides the centre-of-mass energy $\sqrt{s}$ is the luminosity $\mathcal{L}$ which is closely connected to the number of collisions. The luminosity of a head-on collision of two gaussian beams with a cross-section area $A = 4\pi\sigma_x\sigma_y$ is defined as

$$\mathcal{L} = \frac{N_1 N_2 f N_b}{4\pi\sigma_x\sigma_y}, \tag{3.1}$$

where N_1 and N_2 denote the number of particles in the colliding bunches of the two beams, f the revolution frequency and N_b the number of bunches per beam [22]. For physics analyses, the integrated luminosity

$$\mathcal{L}_{int} = \int_0^T \mathcal{L}(t')dt' \tag{3.2}$$

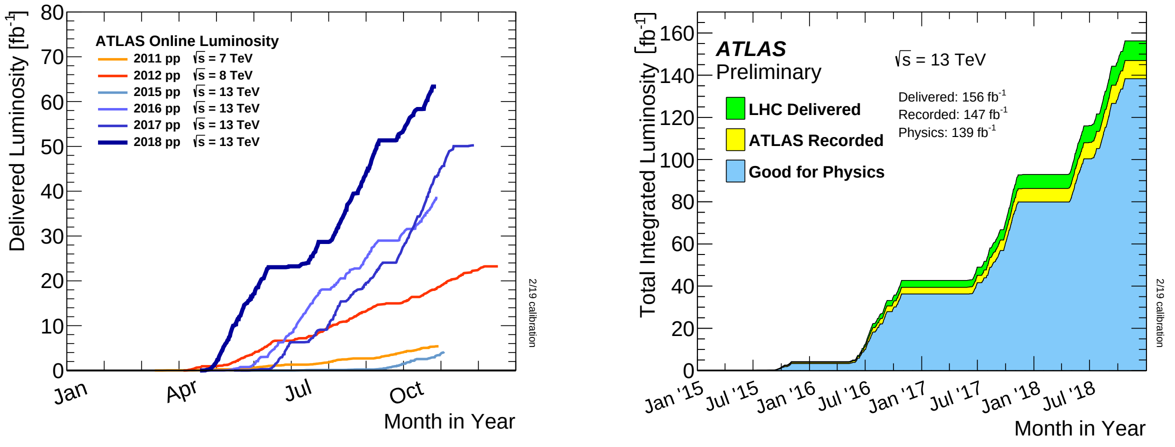

Figure 3.2.: Cumulative luminosity delivered per year (left) and total integrated luminosity of Run 2 (right) [23].

is an important parameter, as it acts as a proportionality factor between the number of events N_p in a certain time interval and the cross section of the respective process σ_p.

$$N_p = \mathcal{L}_{int} \cdot \sigma_p \tag{3.3}$$

The cumulative luminosity delivered by the LHC per year of operation and the total integrated luminosity of Run 2 can be seen in Figure 3.2. Run 1 delivered a total integrated luminosity of $24.9\,\text{fb}^{-1}$ and Run 2 concluded with $139\,\text{fb}^{-1}$ of data recorded by the ATLAS detector and meeting the quality standards for physics analyses.

3.2. The ATLAS Experiment

The ATLAS detector is a general-purpose detector with a height of 25 m and a length of 44 m and is the largest of the four main detectors at the LHC [17]. Section 3.2.1 introduces the coordinate system used by ATLAS, and Section 3.2.2 describes the structure of the detector and its subsystems. Section 3.2.3 provides information on the reconstruction of measured particles.

3.2.1. The Coordinate System

The nominal interaction point defines the origin of the coordinate system used to describe event kinematics in the ATLAS detector. The z-axis is defined by the direction of the proton beams, the y-axis points upwards and the x-axis points towards the centre of the LHC. The azimuthal angle ϕ is measured in the xy-plane, which is also called the transverse plane, and the polar angle θ describes the opening angle from the z-axis.

To describe the detector and event kinematics, polar coordinates r and ϕ are used in the transverse plane. Along the beam direction, the rapidity y, defined as

$$y = \frac{1}{2} \ln \left(\frac{E + p_z}{E - p_z} \right), \tag{3.4}$$

is used. For light particles which have a small mass with respect to their energy, the pseudorapidity η, defined as

$$\eta = \ln \left(\tan \frac{\theta}{2} \right), \tag{3.5}$$

equals the rapidity and is used instead.
The distance between particles is measured via the angular distance

$$\Delta R = \sqrt{(\Delta\phi)^2 + (\Delta\eta)^2}. \tag{3.6}$$

3.2.2. The Detector

A drawing of the ATLAS detector can be seen in Figure 3.3. The detector is forward-backwards symmetric with respect to the interaction point and consists of three major subsystems, the Inner Detector (ID), the calorimeter system and the muon system.

Inner Detector

The ID is the subsystem closest to the beam pipe, consisting of the Pixel Detector, the Semiconductor Tracker (SCT) and the Transition Radiation Tracker (TRT). During the first long shutdown in 2013/14, the Insertable B-Layer (IBL) was added to the Pixel Detector as a new innermost layer to ensure good tracking performance for the increased luminosity and therefore higher radiation of Run 2 [24].
The task of the ID is to measure the trajectory, momentum and charge of electrically charged particles and it is therefore immersed in a 2 T solenoidal magnetic field. The Pixel Detector and the SCT consist of silicon pixel and microstrip layers respectively for the measurement of discrete points of the particle trajectories. The TRT, the outermost layer of the ID, consists of layers of gaseous straw tubes with transition radiation material in between to allow for continuous track measurements. Overall, the ID provides particle track reconstruction for a pseudorapidity of $|\eta| < 2.5$ with an enhanced momentum measurement and electron identification for $|\eta| < 2.0$.

Calorimeter System

The calorimeter system consists of electromagnetic and hadronic calorimeters which measure the energy of the different particles produced in a collision. The electromagnetic calorimeter uses liquid Argon (LAr) as active material and is divided into a barrel part, covering a range of $|\eta| < 1.475$, and end-caps for the range of $1.375 < |\eta| < 3.2$. In the $|\eta| < 2.5$ region, which is also covered by the ID, the calorimeter consists of three layers to allow for precise

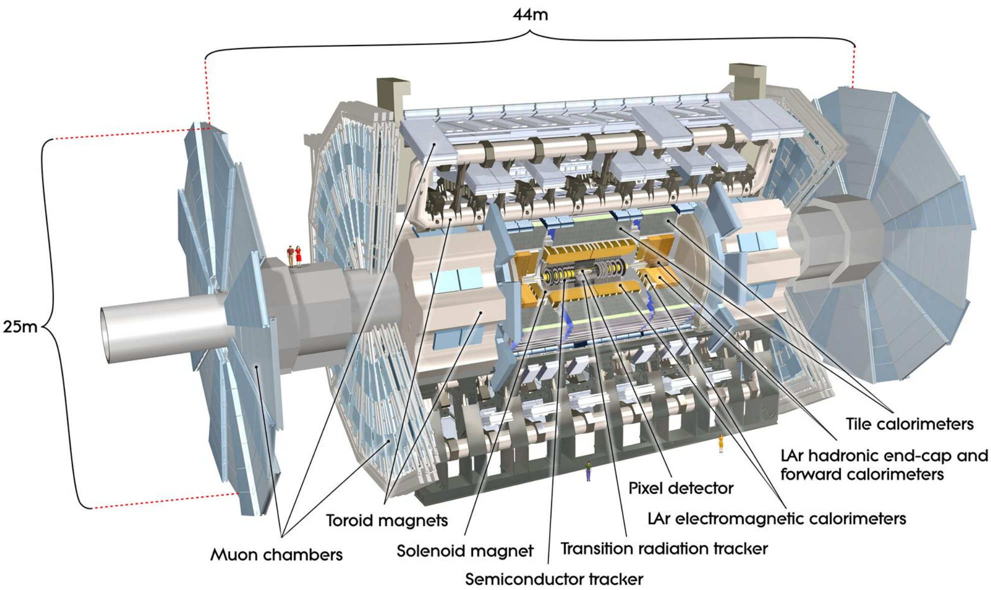

Figure 3.3.: Overview of the ATLAS detector [17].

measurements of electron and photon energies and positions, whereas the outer $|\eta|$ regions only consist of two layers, leading to a coarser resolution. The cylindrical shape leads to full coverage in the azimuthal angle ϕ, but there is a crack region at the transition from the barrel to the end-cap region at $1.37 < |\eta| < 1.52$ where electrons are not properly measured. The hadronic calorimeter system is located around the electromagnetic calorimeter. It consists of a tile calorimeter, which is a sampling calorimeter that uses steel as absorber material and covers a range of $|\eta| < 1.7$, and LAr end-cap calorimeters covering a range of $1.5 < |\eta| < 3.2$. The LAr forward calorimeters, which are embedded in the end-cap calorimeters closely around the beam pipe, provide electromagnetic and hadronic energy measurements in a range of $|\eta| < 4.9$. This coverage of a large pseudorapidity range allows for precise measurements of missing transverse momentum, which is important to reconstruct the presence of neutrinos in a collision event.

Muon System

The muon system is the outermost layer of the ATLAS detector. It consists of spectrometers, which surround the calorimeter system in the barrel region and are orientated perpendicularly to the beam pipe in the end-cap regions, and superconducting air-core toroid magnets which bend the muon tracks for momentum measurements. Monitored Drift Tubes (MDT) are used to measure the muon trajectories over the whole range of $|\eta| < 2.7$ covered by the muon system. In the innermost part of the system, Cathode Strip Chambers (CSC) cover the pseudorapidity range of $2.0 < |\eta| < 2.7$, as they are better suited for the high impact rates expected in this area.

The muon system also includes a trigger system, consisting of Resistive Plate Chambers (RPC) in the barrel region and Thin Gap Chambers (TGC) in the end-cap region, which cover a region of $|\eta| < 2.4$ and measure the muon position in the direction orthogonal to the tracking of the MDTs and CSCs.

Trigger System

Due to the high luminosity of the LHC which results in multiple collision events per bunch crossing and the collision frequency of 40 MHz, not all measured events can be recorded. Therefore, only events passing certain trigger conditions are read out and kept for physical analyses. The trigger system used by ATLAS consists of two consecutive event-selection levels [25]. The first level (L1) trigger is hardware-based and uses the information from the muon system and the calorimeters to sort through the events at the collision frequency of 40 MHz. Events that are selected by the L1 trigger are further analysed by the software-based High-Level Trigger (HLT), which also takes information from the ID into account and reduces the event rate to approximately 1 kHz. Events that pass the HLT selection are written to the data storage systems.

3.2.3. Object Reconstruction

The information gathered by the subdetectors are combined to identify individual particles and to determine their properties such as energy, momentum and direction of flight in terms of η and ϕ.

Electrically charged particles are deflected in the magnetic field of the ID, allowing for momentum measurement and determination of whether a particle carries a positive or a negative charge. Photons and neutrinos are not detected in the ID, but the photons are measured in the adjacent electromagnetic calorimeter. Electrons and photons produce electromagnetic showers in the calorimeter, depositing all of their energy in the process. The energy of hadrons is measured in the hadronic calorimeter and their spatial distribution is used to cluster the hadrons into jets. Muons pass through the calorimeters and are measured in the muon spectrometer, where their trajectory is again deflected by a magnetic field for momentum measurements. The presence of neutrinos is reconstructed from missing transverse momentum, as they pass through the whole detector without interaction. The colliding protons do not carry transverse momentum, therefore, the transverse momenta of the particles produced in the interaction have to add up to zero as well. An imbalance indicates the existence of at least one neutrino.

The precise measurement of the particle trajectories in the ID also allows for reconstruction of the nominal interaction point and hence for the identification of primary and secondary vertices. This information is used in the identification of jets originating from hadrons consisting of b-quarks, as those hadrons have a relatively long lifetime. Algorithms used to identify the so-called b-jets therefore take into account the displacement of vertices from the nominal interaction point, together with other distinct features of b-jets such as their high mass.

4. Data and Monte Carlo samples

The different interaction processes occuring in collision events are modeled with Monte Carlo (MC) simulations in order to compare the collected data to the predictions. Different MC samples are used to model the signal process and background processes, i.e. SM processes producing event signatures similar to the signal process. In Section 4.1, the background processes considered for the analysis are discussed. Section 4.2 provides general information on the data and MC samples used for this analysis.

4.1. Event Signatures

The final state of the signal process is characterized by the presence of two leptons of the same flavour and opposite charge as well as at least one b-jet (cf. Section 2.2.2). Four SM processes producing similar final states are considered as background processes for this analysis. Exemplary decay channels for all of these processes are presented in Figure 4.1 and Figure 4.2. The largest background contribution is expected from $t\bar{t}$ decays with both $W^{\pm}$ bosons decaying leptonically. A single top quark produced with an associated, leptonically decaying W^{-} boson can similarly produce a dilepton final state, and a $Z \to \ell\ell$ decay process with the Z boson being radiated off a b-quark contains a b-jet in the final state.

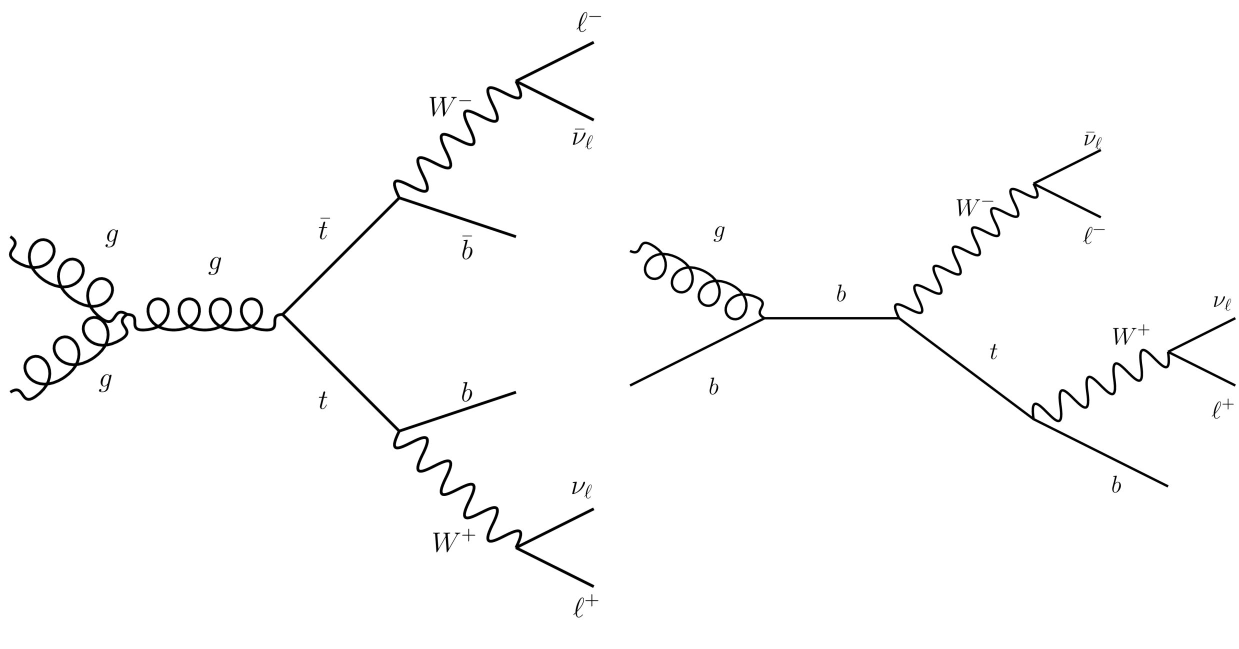

Figure 4.1.: Example diagrams of the considered background processes. Shown are a dileptonic $t\bar{t}$ decay (left) and an event tW production with both $W^{\pm}$ bosons decaying leptonically (right).

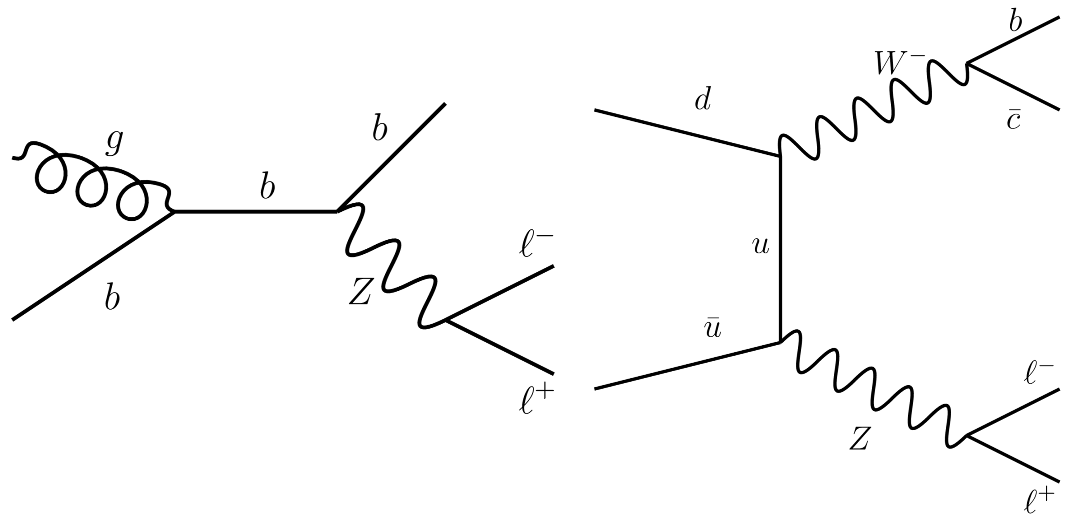

Figure 4.2.: Example diagrams of the considered background processes. Shown are a b quark radiating a Z boson (left) and a diboson decay with a hadronically decaying W^- boson and a leptonically decaying Z boson (right).

The diboson background includes all processes involving two bosons of the weak interaction, with the example of a hadronically decaying W^- boson in association with a leptonically decaying Z boson being presented in Figure 4.2.
Another source for background events is the so-called multijet background, consisting of events with at least one jet being misidentified as a lepton by the detector. This background is not modelled with MC samples but estimated from real data, as described in Section 6.2.

4.2. Sample Information

The data samples used for this analysis are generated from the data collected by the ATLAS detector in 2015 and 2016 at a centre-of-mass energy of $\sqrt{s} = 13\,\text{TeV}$ with an integrated luminosity of $36.2\,\text{fb}^{-1}$. The dataset collected in 2017 and 2018 provides higher event statistics but requires more computation time. The event statistics are the only difference between the datasets, therefore, the results of the analysis carried out with the 2015/16 data are expected to be applicable to the full Run 2 dataset as well.
MC samples are used to model the signal process and the most important background processes. The generation of MC samples is split into the perturbative calculation of the matrix element and the simulation of the hadronization process. As a final step, the response of the ATLAS detector is simulated.
Table 4.1 provides an overview of the generated processes and the programmes used for the different simulation steps, including the PDF sets used by the matrix element (ME) generators.

Background samples

The $t\bar{t}$ and single-top quark samples are generated at leading order with the POWHEG-BOX [26] v2 matrix-element generator using NNPDF3.0nlo [13]. PYTHIA 8.230 [27] is used for the parton-shower simulation which is finalized by EVTGEN v1.6.0 [28]. The Z→ $\ell\ell$ samples, referred to as Z$\ell\ell$ in the following, are generated at next-to-leading order using SHERPA 2.2.1 [29] with PDFs being calculated with NNPDF3.0nnlo [13]. The diboson samples are generated at next-to-leading order with SHERPA 2.2.1 and SHERPA 2.2.2 using NNPDF3.0nnlo [13]. The parton-shower simulation is also done with the respective SHERPA version for both the Z$\ell\ell$ and diboson samples.
For all background processes, a full detector simulation, referred to as FullSim, is done using GEANT4 [30].

Signal samples

For the Z'→ $\ell\ell$ signal process, separate MC samples are generated for Z' masses of 0.5 TeV, 1 TeV and 2 TeV. The signal Z'→ $\ell\ell$ samples, referred to as Z'$\ell\ell$ in the following, are generated at leading order by MadGraph5_aMC@NLO [31] with NNPDF3.0nlo using cross sections for the production of a Z' in association with one or two jets originating from b or s quarks. The 5-flavour scheme is used, meaning that b-quarks are treated as proton partons and a b-quark PDF is included in the calculation of the cross section $\sigma(pp \to Z' + j/jj)$. The parton-shower simulation is done with PYTHIA 8.245 and EVTGEN v1.7.0. As the ME generator explicitly generates a Z' with associated jets, CKKW-L [32] merging is used with a merging scale of 30 GeV in order to remove the overlap between the ME calculation and the parton-shower modelling.
A dynamic factorisation and renormalisation scale of $0.5M_{\mathrm{T}}$ is used, with M_{T} being the scalar sum of the transverse masses of all particles and partons in the final state of an event. The model parameters governing the coupling of the Z' to the different fermions are left at the default values of the used model. For the coupling of the Z' to $b\bar{b}$ and $t\bar{t}$, the model parameters are set to 0.5. The parameter for the Z' coupling to $s\bar{b}$ or $b\bar{s}$ is set to $|V_{cb}| \cdot 0.5$ and the parameter for the coupling to $s\bar{s}$ is set to $|V_{cb}|^2 \cdot 0.5$. The model parameters for the coupling to electrons and muons are both set to 0.5. The cross sections are recalculated for the calculation of exclusion limits (cf. Chapter 8), with the model parameter of either

Table 4.1.: Generators of the MC samples for background and signal processes.

Process	ME generator	ME PDF	Parton shower	Detector simulation
Z$\ell\ell$	SHERPA 2.2.1	NNPDF3.0nnlo	SHERPA	FullSim
$t\bar{t}$	POWHEG-BOX v2	NNPDF3.0nlo	PYTHIA 8 (v8.230)	FullSim
Single top	POWHEG-BOX v2	NNPDF3.0nlo	PYTHIA 8 (v8.230)	FullSim
Diboson	SHERPA 2.2.1/2.2.2	NNPDF3.0nnlo	SHERPA	FullSim
Z'$\ell\ell$	MadGraph 2.9.3	NNPDF3.0nlo	PYTHIA 8 (v8.245)	Atlfast II/FullSim

electrons or muons kept at 0.5 for the respective Z'$\ell\ell$ samples while the parameter for the other lepton flavour is set to zero.
The detector response is simulated with Atlfast II, using a fast simulation algorithm for the simulation of the ATLAS calorimeters in order to reduce computation time [33]. For both the Z'$\rightarrow ee$ and Z'$\rightarrow \mu\mu$ process, one FullSim sample is produced as well with a Z' mass of 1 TeV for a comparison between the different detector simulations (cf. Section 7.1).

5. Object Definition

The various analyses carried out with ATLAS data pose different requirements on the reconstruction of collision events from detector information, regarding for example the background rejection or the reconstruction efficiency of certain particles. Therefore, different algorithms are available for the reconstruction of objects measured by the detector. The object definitions used for this analysis are presented in this chapter.

For the reconstruction of physical objects from measured tracks, a variety of properties of the tracks measured by the different detector parts, such as their position and energy deposition, are taken into account. To identify whether a track originates from the event of interest or from a different collision event occuring during the same bunch crossing, the transverse impact parameter d_0 and the longitudinal impact parameter z_0, describing the displacement of a particle track from the nominal interaction point, are used.
For electrons and muons, a distinction between baseline and signal candidates is made with the signal candidates being a subset of the baseline candidates, passing stricter selection criteria. The baseline leptons are stored in the event samples as they are needed for the estimation of the multijet background, as described in Section 6.2. The selection criteria used for the different physical objects are described in the following. A short summary of the lepton selection criteria can be found in Table 5.1.

Electrons

Baseline electrons are required to have $p_{\mathrm{T}} > 20\,\mathrm{GeV}$ and $|\eta| < 2.47$. The `LooseandBLayerLLH` identification is used, requiring a loose likelihood identification criterion combined with at least one hit recorded in the innermost layer of the ID [34]. Signal electrons additionally need to pass a medium likelihood identification criterion, referred to as `MediumLLH`, as well as the `HighPtCaloOnly` isolation criterion based on calorimeter-based information. To pass the isolation criterion, the energy deposited in a cone of the size $\Delta R = 0.2$ around the electron's cluster position has to be smaller than $\max(0.015\,p_{\mathrm{T}}^{e}, 3.5\,\mathrm{GeV})$. Signal electrons additionally need to satisfy $|z_0 \sin(\theta)| < 0.5\,\mathrm{mm}$ and $|d_0/\sigma(d_0)| < 5.0$.

Muons

Muon candidates are required to have $p_{\mathrm{T}} > 20\,\mathrm{GeV}$ and $|\eta| < 2.5$. Both baseline and signal muons are selected according to the High-p_T criterion, which is optimized for the reconstruction of muons with $p_{\mathrm{T}} > 100\,\mathrm{GeV}$ by requiring at least three hits in the muon system [35]. Signal muons need to additionally pass the track-based `TightTrackOnly_VarRad` isolation criterion, limiting the scalar sum of transverse momenta of all tracks with $p_{\mathrm{T}} > 1\,\mathrm{GeV}$ within a distance of $\Delta R = \min(10\,\mathrm{GeV}/p_{\mathrm{T}}^{\mu}, 0.3)$ to the muon to 6% of the muon's transverse momentum p_{T}^{μ}. Additional requirements on the impact parameters $|d_0/\sigma(d_0)| < 3.0$ and $|z_0 \sin(\theta)| < 0.5\,\mathrm{mm}$ are set for signal muons.

Table 5.1.: Object definition criteria for leptons.

		p_{T}	$\lvert\eta\rvert$	$\lvert z_0 \sin(\theta)\rvert$	$\lvert d_0/\sigma(d_0)\rvert$	Identification	Isolation
Electron	Baseline	$> 20\,\mathrm{GeV}$	< 2.47	-	-	`LooseandBLayerLLH`	-
	Signal	$> 20\,\mathrm{GeV}$	< 2.47	$0.5\,\mathrm{mm}$	5.0	`MediumLLH`	`HighPtCaloOnly`
Muon	Baseline	$> 20\,\mathrm{GeV}$	< 2.5	-	-	High-p_{T}	-
	Signal	$> 20\,\mathrm{GeV}$	< 2.5	$0.5\,\mathrm{mm}$	3.0	High-p_{T}	`TightTrackOnly_VarRad`

Jets

Jets are reconstructed with the particle-flow algorithm, taking into account the energy deposited in the calorimeters as well as momentum measurements of the ID [36]. The anti-k_t algorithm is used to cluster the measured tracks into jets with a cone size of $\Delta R = 0.4$ [37]. The jets are required to have $p_{\mathrm{T}} > 20\,\mathrm{GeV}$, $|\eta| < 4.5$ and to pass a quality criterion ensuring that the jet originates from a proton-proton collision and not from background processes such as air-showers induced by cosmic muons.
To identify jets originating from b-quarks, the b-tagging algorithm DL1r [38] is used with a working point of 85%, meaning that 85% of the jets originating from b-quarks are identified as b-jets. The b-tagging procedure works within a pseudorapidity range of $|\eta| < 2.5$.

Missing transverse momentum

The missing transverse momentum $E_{\mathrm{T}}^{\mathrm{miss}}$ describes the transverse momentum imbalance of an event. The transverse momenta of all particles produced in a collision need to add up to zero, as the colliding protons carry in a very good approximation no transverse momentum. An $E_{\mathrm{T},i}^{\mathrm{miss}}$ term is calculated for each particle type i as the negative sum of the momenta of all reconstructed and calibrated objects of this type [39]. The total $E_{\mathrm{T}}^{\mathrm{miss}}$ of an event is then defined as the sum over all $E_{\mathrm{T},i}^{\mathrm{miss}}$ terms with an additional soft-term being reconstructed from tracks measured by the ID but not associated to any reconstructed object.
Real $E_{\mathrm{T}}^{\mathrm{miss}}$ is caused by neutrinos produced in a collision, as they travel through the detector without interacting, whereas fake $E_{\mathrm{T}}^{\mathrm{miss}}$ is caused by mismeasurements of the transverse momentum of other particles. To distinguish between these two types, the $E_{\mathrm{T}}^{\mathrm{miss}}$ significance $\sigma(E_{\mathrm{T}}^{\mathrm{miss}})$ is calculated from the momentum resolution of all reconstructed particles, with a high $\sigma(E_{\mathrm{T}}^{\mathrm{miss}})$ indicating the presence of real $E_{\mathrm{T}}^{\mathrm{miss}}$.

Overlap removal

As it is possible for one particle-level object to be reconstructed as two different measured objects, a procedure called overlap removal is applied to ensure that only one of the identified particles is kept. The choice of which particle is being kept depends on the properties of the different candidates, according to rules listed in the following. Subsequent steps only consider particles that survived the previous removal steps. Baseline leptons are considered for all removal steps involving electrons and muons.

1. For two electrons sharing a track in the ID, the electron with higher p_{T} is kept.
2. Muons reconstructed from calorimeter information are rejected against electrons sharing the track in the ID.
3. Electrons are rejected against muons reconstruced from muon-system information sharing the track in the ID.
4. Jets are rejected against electrons within $\Delta R < 0.2$, with b-tagged jets only being rejected against electrons with $p_{\mathrm{T}} > 100\,\mathrm{GeV}$.
5. Jets are rejected against muons within $\Delta R < 0.2$ or against muons with ID tracks matching a ghost-track of the jet. Jets identified as b-jets are not rejected against muons.

6. Background Modelling and Validation

The general idea of a direct search for new physics is to compare the collected data to the prediction of the known SM processes resulting in similar event signatures in order to search for an excess in data events. It is therefore important to validate that the expected background processes are well modelled.
The event selection used as a starting point for the analysis presented in this thesis is defined in Section 6.1. Section 6.2 provides information on the modelling of the so-called multijet background, which is estimated from the data samples instead of being modelled by MC samples. Studies of the agreement between data and MC predictions for two regions with different event selection criteria are presented in Section 6.3 and Section 6.4 respectively.

6.1. Preselection region

The final state of the Z' signal processes is characterized by two leptons of opposite charge and same flavour as well as the presence of at least one b-jet (cf. Section 2.2.2). Therefore, the analysis is carried out for two different channels, referred to as muon channel and electron channel respectively, both of which require exactly two signal leptons of the respective flavour, no signal leptons of the other flavour and at least one b-tagged jet. A requirement on the lepton charge is not used as it was found to have no significant impact on the number of selected events.
The invariant mass of the two leptons $M(\ell\ell)$ is required to be larger than 130 GeV in order to exclude the Z-boson resonance at 91 GeV. The leptons are additionally required to have a transverse momentum $p_{\mathrm{T}} > 65\,\mathrm{GeV}$, and the jets need to satisfy $p_{\mathrm{T}} > 30\,\mathrm{GeV}$.
Jet cleaning is applied, meaning that events containing jets not passing the `LooseBad` quality criterion [40] after the overlap removal procedure are vetoed. For the electron channel, events are also vetoed if the energy cluster of one of the signal electrons lies in the pseudorapidity range $1.37 < |\eta^{e}_{\mathrm{cl}}| < 1.52$, as electrons are not properly measured by the calorimeter system in this region (cf. Section 3.2.2). Events in the muon channel are vetoed if one of the muons is flagged as 'bad', indicating a significantly worse momentum resolution for the muon in comparison to unflagged muons. A summary of the applied event selection criteria, defining a preselection region used as a basis for a later signal region definition, is given in Table 6.1.

The lowest unprescaled dielectron triggers and single-muon triggers, listed in Table 6.2, are used for the event selection in the respective channel. The dielectron-trigger names provide information on the E_{T} requirement, the identification and the isolation criteria applied for both electrons. `lhloose` and `lhvloose` indicate a loose and very loose likelihood identification respectively, with `nod0` indicating that the d_0 information is not used for the identification. `L12EM10VH` specifies the applied L1 trigger, requiring two electrons with an

Table 6.1.: Event selection criteria of the preselection region for the electron and muon channel.

Electron Channel	Muon Channel
two signal electrons	two signal muons
no signal muons	no signal electrons
passed dielectron trigger	passed single-muon trigger
$1.37 < \lvert\eta^e_{\text{cl}}\rvert < 1.52$	bad muon veto
electron $p_{\text{T}} > 65\,\text{GeV}$	muon $p_{\text{T}} > 65\,\text{GeV}$
$\text{M}_{ee} > 130\,\text{GeV}$	$\text{M}_{\mu\mu} > 130\,\text{GeV}$
jet cleaning	jet cleaning
jet $p_{\text{T}} > 30\,\text{GeV}$	jet $p_{\text{T}} > 30\,\text{GeV}$
at least one b-tagged jet	at least one b-tagged jet

Table 6.2.: Dielectron and single-muon triggers applied in the preselection region.

Dielectron triggers	Single-muon triggers
`HLT_2e12_lhloose_L12EM10VH`	`HLT_mu26_imedium`
`HLT_2e17_lhvloose_nod0`	`HLT_mu26_ivarmedium`
`HLT_2e24_lhvloose_nod0`	`HLT_mu50`

$E_{\text{T}} > 10\,\text{GeV}$, using a hadronic core isolation and varying the threshold dependent on η to account for energy losses. The muon trigger names specify the E_{T} requirement as well, followed by the applied isolation criterion. The `imedium` criterion requires the p_{T} within a cone of $\Delta R = 0.3$ around the muon to be below 6% of the muon's p_{T}. For the `ivarmedium` criterion, the definition of the cone size is changed to $\Delta R = \min(10\,\text{GeV}/p^{\mu}_{\text{T}}, 0.3)$ and the `HLT_mu50` trigger requires no isolation. Only one of the applied triggers needs to be fulfilled for an event to pass the event selection of the preselection region.
The composition of the MC simulated background in the preselection region for the electron channel and the muon channel is presented in Figure 6.1 and Figure 6.2 respectively. The composition is very similar for both lepton channels with the $t\bar{t}$ decay being the predominant process, accounting for almost 81% of all background events. The estimation of the data-driven multijet background and a validation of the $t\bar{t}$ background are presented in the following.

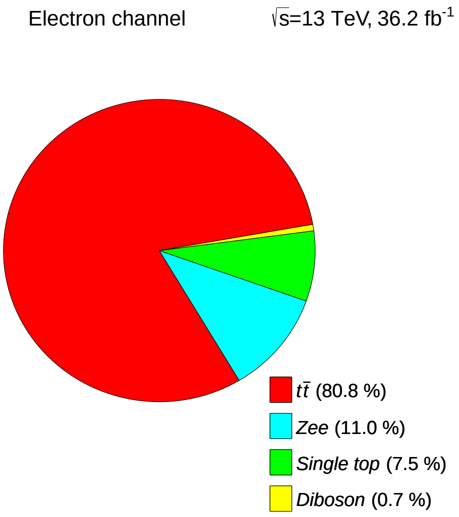

Figure 6.1.: Event yields of the MC simulated processes in the preselection region for the electron channel.

Table 6.3.: Event yields per process for the electron channel.

Process	Event Yield
Diboson	108
Single top	1190
Zee	1745
$t\bar{t}$	12800

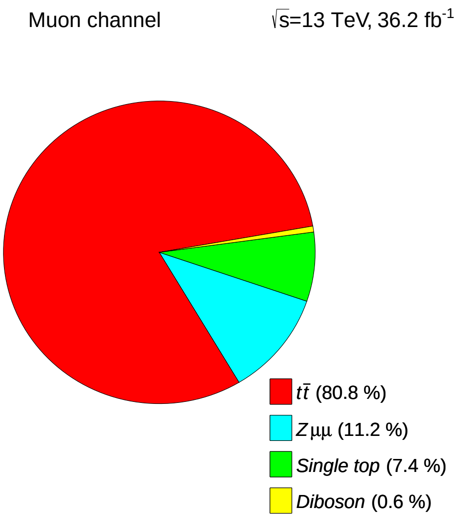

Figure 6.2.: Event yields of the MC simulated processes in the preselection region for the muon channel.

Table 6.4.: Event yields per process for the muon channel.

Process	Event Yield
Diboson	87
Single top	1017
$Z\mu\mu$	1544
$t\bar{t}$	11120

6.2. The Multijet Background

It is possible for a jet in the final state of a collision event to pass the lepton candidate selection criteria (cf. Chapter 5). These so-called fake leptons are a non-negligible source for background in the electron channel and their contribution is therefore estimated using a data-driven technique called the Matrix Method, as described in Ref. [41]. Other sources contributing to the multijet background are electrons originating from photon conversions or hadron decays, both of which are also accounted for by the data-driven approach but not explicitly mentioned in the following.
For the muon channel, the contribution of fake leptons is expected to be lower than for the electron channel, as the muon identification uses information from the muon system, the outermost layer of the ATLAS detector, whereas jets are expected to deposit all of their energy in the hadronic calorimeter. Therefore, the multijet background for the muon channel originates almost exclusively from muons produced in hadron decays. For the analysis presented in this thesis, the multijet background is not considered for the muon channel. In Section 6.2.1, the theory behind the Matrix Method is presented, followed by the efficiencies that were obtained for real and fake electron identification in Section 6.2.2.

6.2.1. The Matrix Method

The idea behind the Matrix Method is to connect the number of events containing fake electrons to quantities that are accessible in data samples in order to calculate a fake-background estimation. The accessible quantities which are used are the number of events with loose and tight electrons respectively, where tight electrons are those candidates that pass the signal selection while loose electrons are only required to pass the baseline selection consisting of a less strict identification criterion and no isolation criterion (cf. Chapter 5).
The real efficiency r and fake efficiency f, which describe the fraction of loose electron candidates passing the tight electron selection for real and fake electrons respectively, can be written as

$$r = \frac{N^{\text{real}}_{\text{tight}}}{N^{\text{real}}_{\text{loose}}}, \qquad f = \frac{N^{\text{fake}}_{\text{tight}}}{N^{\text{fake}}_{\text{loose}}}. \tag{6.1}$$

With these efficiencies, the number of events with tight electrons N_T and loose electrons N_L can be expressed in terms of the number of events with real electrons N_R and fake electrons N_F.

$$\begin{bmatrix} N_{TT} \\ N_{TL} \\ N_{LT} \\ N_{LL} \end{bmatrix} = \begin{pmatrix} r_1 r_2 & r_1 f_2 & f_1 r_2 & f_1 f_2 \\ r_1(1-r_2) & r_1(1-f_2) & f_1(1-r_2) & f_1(1-f_2) \\ (1-r_1)r_2 & (1-r_1)f_2 & (1-f_1)r_2 & (1-f_1)f_2 \\ (1-r_1)(1-r_2) & (1-r_1)(1-f_2) & (1-f_1)(1-r_2) & (1-f_1)(1-f_2) \end{pmatrix} \begin{bmatrix} N_{RR} \\ N_{RF} \\ N_{FR} \\ N_{FF} \end{bmatrix} \tag{6.2}$$

As the analysis requires events with a dilepton final state, the efficiencies are calculated separately for the p_{T}-leading electron, which is denoted by the subscript 1, and the p_{T}-subleading electron, which is denoted by the subscript 2. For the event numbers N, the first subscript

classifies the status of the leading electron and the second subscript classifies the subleading electron. It is important to note that N_L refers to the number of events with loose electrons which do not pass the tight selection so that each event is only counted once for the lefthand side of Equation (6.2).
It can be seen in Equation (6.2) that the contribution of events with fake electrons to the signal selection is given by

$$N_{TT}^{\text{fake}} = r_1 f_2 \cdot N_{RF} + f_1 r_2 \cdot N_{FR} + f_1 f_2 \cdot N_{FF}. \tag{6.3}$$

Events with one real and one fake electron originate mostly from events containing one leptonically decaying $W^{\pm}$ boson and an additional, misidentified jet. By inverting the matrix in Equation (6.2), the numbers of events with fake electrons can again be expressed in terms of events with tight and loose leptons, meaning that N_{TT}^{fake} can be calculated as

$$\begin{aligned} N_{TT}^{\text{fake}} = \alpha[(r_1 r_2 (f_1 + f_2) + f_1 f_2 (1 - r_1 r_2) - r_1 f_2 - r_2 f_1) N_{TT} \\ +(r_1 r_2 f_2 (1 - f_1)) N_{TL} \\ +(r_1 r_2 f_1 (1 - f_2)) N_{LT} \\ -(r_1 r_2 f_1 f_2) N_{LL}], \end{aligned} \tag{6.4}$$

with $\alpha = ((r_1 - f_1)(r_2 - f_2))^{-1}$.

6.2.2. Electron Selection Efficiencies

The real efficiency r for the p_{T}-leading and p_{T}-subleading electron is determined from the MC Zee samples. A loose electron candidate has to pass the `LooseAndBLayerLLH` identification and no isolation criterion, whereas a tight electron candidate has to additionally pass the `MediumLLH` identification and `HighPtCaloOnly` isolation criterion (cf. Table 5.1). All electron candidates are further required to have a distance of $\Delta R < 0.1$ to a truth MC electron, referring to a MC generated electron without having the detector simulation applied, in order to assure that only real electrons contribute to the calculation of the real efficiency. The real efficiencies obtained for the leading and subleading electron binned in $|\eta|$ and p_{T} are presented in Figure 6.3. The subleading electron suffers from low event statistics in the region of high transverse momentum and $|\eta|$, leading to large statistical uncertainties. For transverse momenta around 250 GeV, the real efficiencies of both electrons exhibit a rather steep decrease. This can be explained by the chosen `HighPtCaloOnly` isolation criterion, setting the allowed energy deposition around the electron to $\max(0.015\, p_{\text{T}}^{e},\ 3.5\,\text{GeV})$ (cf. Chapter 5). With increasing transverse momentum, the energy deposition of an electron increases as well, decreasing the fraction of electrons passing the fixed threshold of 3.5 GeV. For electrons with a p_{T} above 230 GeV, the threshold for the allowed energy deposition becomes p_{T}-dependent, which increases the fraction of electrons passing the isolation. Overall, the real efficiency is slightly higher for the leading electron than for the subleading electron but stays well over 90% for both electrons in most p_{T} and $|\eta|$ regions.

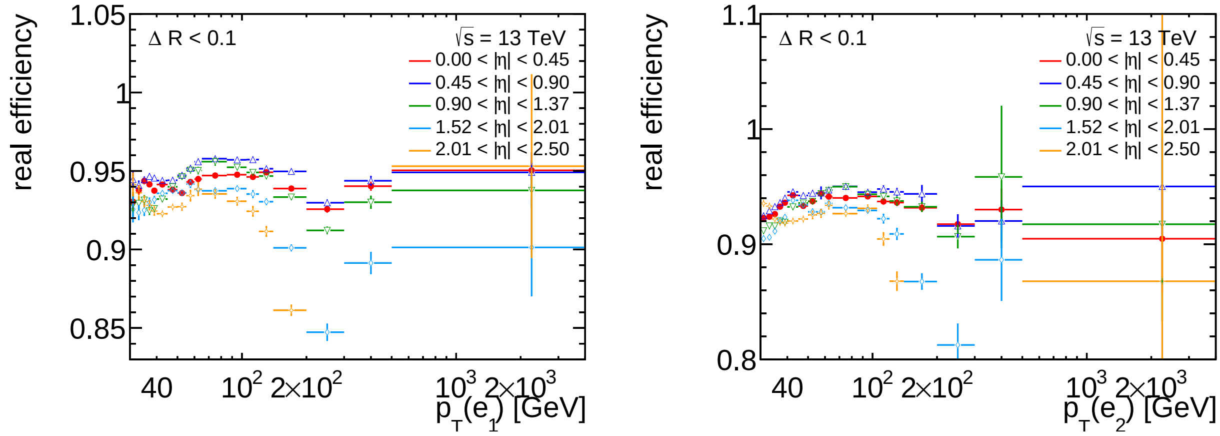

Figure 6.3.: Real efficiency of the leading electron (left) and subleading electron (right).

The fake efficiency f is measured in real data by applying selection criteria that suppress the contribution of real electrons. Dedicated samples are needed for this, as the fake efficiencies are calculated from single-electron control regions, which require a different derivation of the data samples than the dilepton selection. These samples were not available for this thesis, therefore the fake efficiencies calculated for a SM analysis of Drell-Yan processes in the high dilepton invariant mass region are used. The fake efficiencies are calculated using the same identification and isolation criteria for the definition of loose and tight electrons as this analysis. As the fake efficiencies are measured in a single-electron control region, the same fake efficiency has to be applied for the leading and subleading electron. A 2D-histogram of the used fake efficiency binned in p_{T} and $|\eta|$ can be found in Figure A.1.

6.3. Top Background Validation

The largest source of background events with a similar final state as the Z' signal process are dileptonic $t\bar{t}$ decays (cf. Section 6.1). Together with the single-top decays, background processes involving top-decay processes account for over 85% of the background events in both lepton channels. It is therefore important to check whether these background processes are well modelled by the used MC samples. Section 6.3.1 describes the definition of the top control region, and the results of the background validation are presented in Section 6.3.2.

6.3.1. Top Control Region Setup

The top control region is chosen to be orthogonal to all signal regions, as the event yield in the MC samples for background processes is compared to the event yield of the data sample. As the signal regions of this analysis require two leptons of the same flavour, events in the top control region are required to contain exactly one electron and one muon. The leptons are further required to carry opposite electric charge to suppress the contribution of

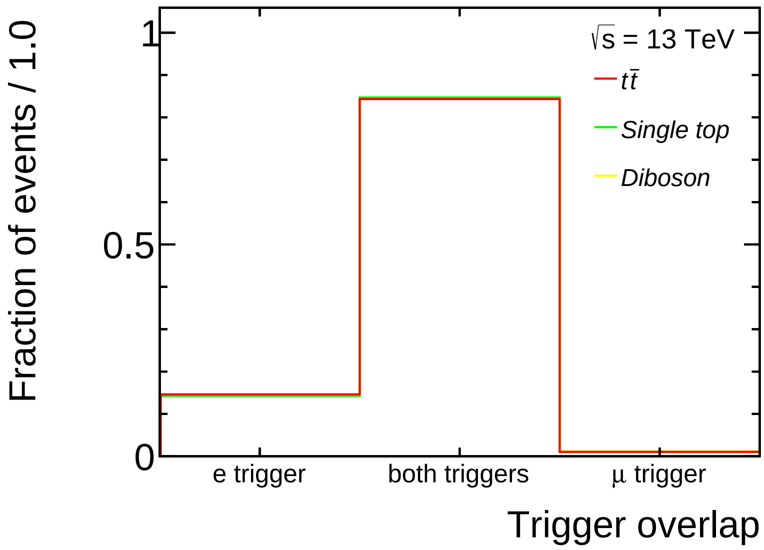

Figure 6.4.: Overlap of the MC events chosen in the top control region using single-electron triggers and single-muon triggers respectively.

the diboson and multijet background. The other event selection criteria of the preselection region (cf. Table 6.1) are kept in order to stay as close to that region as possible.
The available single-electron triggers are prescaled, meaning that not every event measured with the ATLAS detector that fulfils those trigger requirements is recorded and the event yield of the data sample has to be multiplied with prescale factors. Therefore, the single-electron triggers cannot be used simultaneously with the single-muon triggers for selecting data events. A list of the used single-electron triggers with the respective prescale factors can be found in Table A.1.
Both top control regions obtained by using either single-electron or single-muon triggers are discussed in the following. The overlap between the MC generated background events chosen with single-electron and single-muon triggers respectively is presented in Figure 6.4. Out of all events passing a trigger requirement, about 85% pass both single-lepton triggers, with most of the remaining 15% of events being chosen by the single-electron triggers only. It can be therefore concluded that the event compositions obtained with the different triggers are very similar.

The multijet background is included in the top control region. As the multijet background is not considered for the muon channel (cf. Section 6.2.1), the real and fake efficiency of the muons are set to one and zero respectively ($r_\mu = 1,\ f_\mu = 0$), reducing the dilepton Matrix Method to the one dimensional case with one electron only, where

$$N_T^{\text{fake}} = \frac{f_e}{r_e - f_e}[(r_e - 1)N_T + r_e N_L]. \tag{6.5}$$

6.3.2. Top Background Validation Results

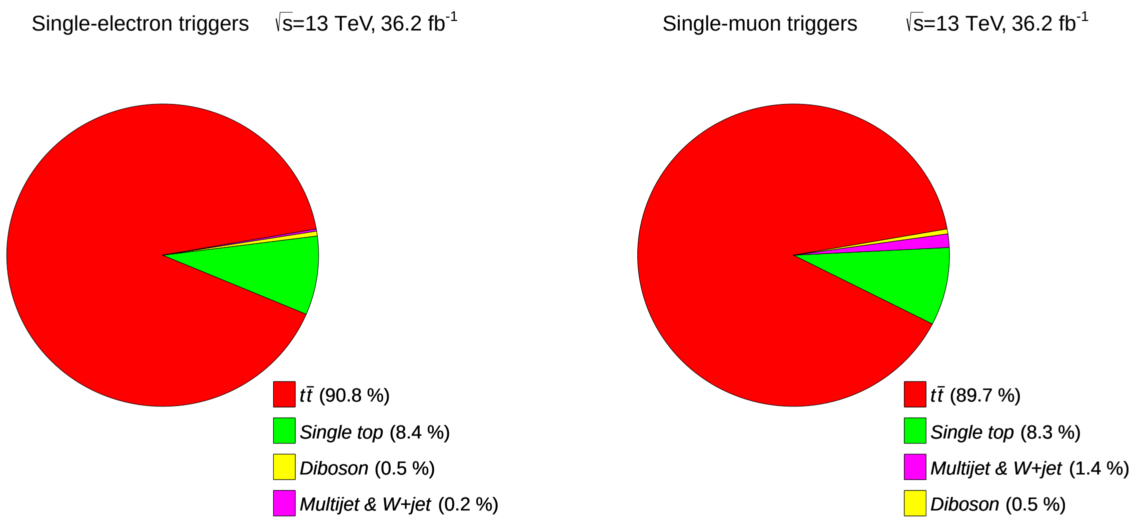

Figure 6.5.: Composition of MC events in the top control region obtained using single-electron triggers (left) and single-muon triggers (right).

Figure 6.5 shows the event composition in the top control region with the respective event yields listed in Table 6.5. For both the single-electron and the single-muon trigger, the fraction of $t\bar{t}$ and single-top events lies around 98%, meaning that the applied event selection is suitable for a validation of the top-background modelling.
For the MC simulated background processes and the data, the event yield obtained with the single-electron triggers is about 1.2 times higher than the event yield obtained with the single-muon triggers, in accordance with the overlap of selected events between the triggers (cf. Figure 6.4). For the multijet background, the event yield obtained with the single-electron

Table 6.5.: Event yields per process in the top control region obtained with single-electron triggers and single-muon triggers respectively.

Process	Single-electron triggers	Single-muon triggers
Diboson	137	113
Multijet	60	316
Single top	2225	1819
$t\bar{t}$	24010	19580
Total background	26390	21830
Data	25510	21300

triggers is lower than expected. As the multijet background is estimated from data, the prescale factors of the single-electron triggers have to be taken into account. The ratio of events with loose and tight electrons recorded with the single-electron triggers does not necessarily equal the ratio within all events measured by the ATLAS detector. This ratio is important, as an event with a tight electron can result in a negative event weight (cf. Equation (6.5)). Therefore, the estimation of the multijet background with the single-electron triggers is expected to be imprecise and strong fluctuations of the multijet background can be seen in the plots presented in Appendix A.2.

The invariant mass distributions of the two leptons obtained with the different triggers are presented in Figure 6.6. The yield of the MC samples agrees well with the data for both triggers, but the statistical uncertainties of the data points are visibly larger for the event selection using the single-electron triggers. This is a consequence of the triggers being prescaled, leading to significantly lower event statistics for the data sample.
The distributions of $E_{\mathrm{T}}^{\mathrm{miss}}$, p_{T} of the leptons and of the p_{T}-leading b-jet and jet multiplicities obtained with the single-muon triggers are presented in Figure 6.7. Although the statistical uncertainties of both the MC and data samples increase for regions of high $E_{\mathrm{T}}^{\mathrm{miss}}$ and p_{T}, the agreement of the event yields remains sufficiently well. The jet multiplicity peaks at two jets per event as it is expected for dileptonic $t\bar{t}$ events. The b-tagging working point of 85% results in a high amount of $t\bar{t}$ events with two identified b-jets, being lowered visibly below the expected fraction of $\approx$ 72% of all events with two b-jets by the presence of forward-jets with $|\eta| > 2.5$, for which the b-tagging algorithm cannot be applied.

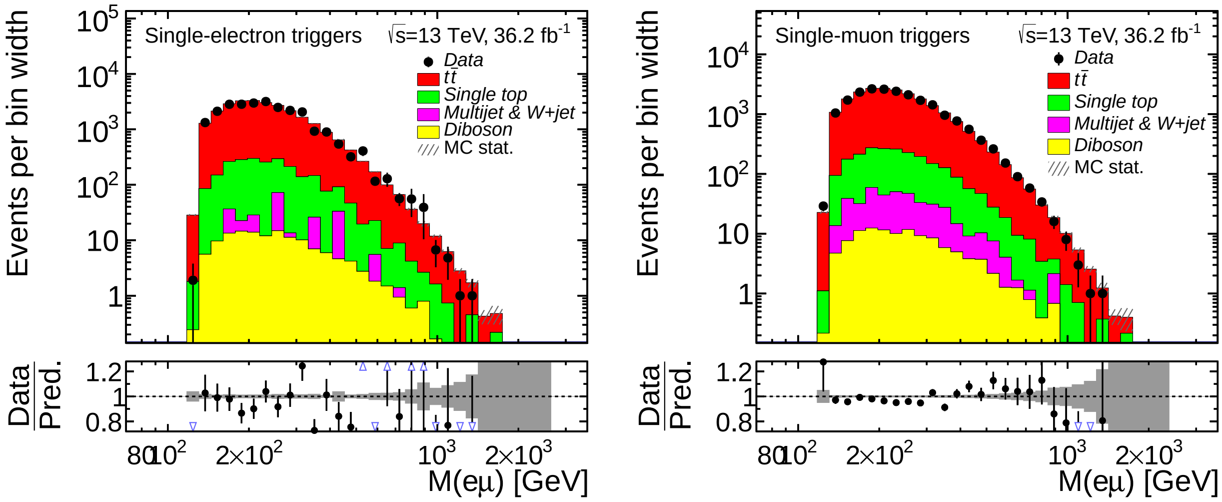

Figure 6.6.: Dilepton invariant mass distribution in the top control region obtained using single-electron triggers (left) and single-muon triggers (right).

The same variables obtained with the single-electron trigger as well as additional variables for both single-lepton triggers can be found in Appendix A.2. The larger statistical uncertainties of the data samples with the single-electron triggers applied become obvious especially in regions with low event yields, but the agreement between data and MC remains fairly well. Overall, the variables show a good agreement between data and MC within the statistical uncertainties, and it can be therefore concluded that the top background is modelled well by the MC samples.

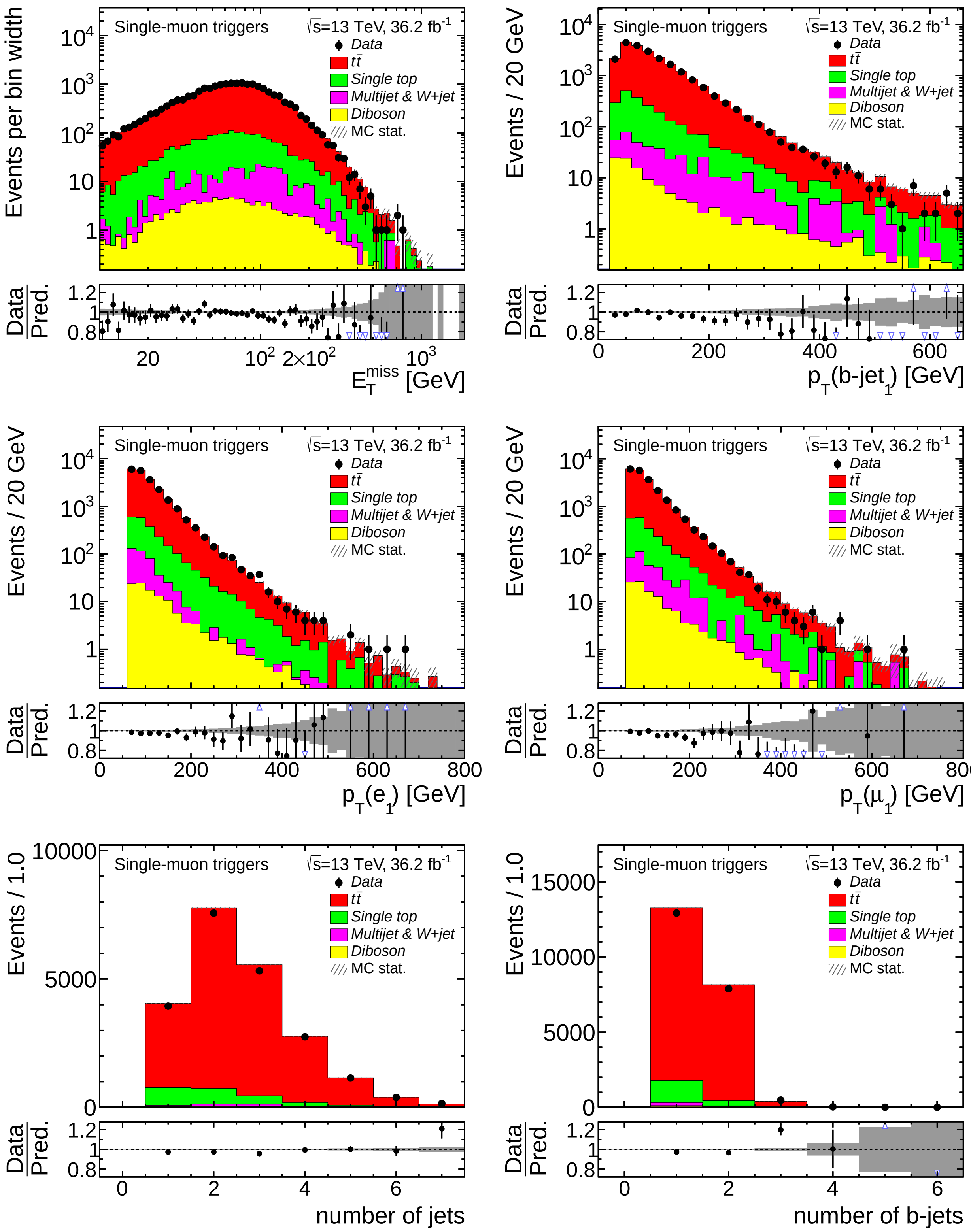

Figure 6.7.: $E_{\mathrm{T}}^{\mathrm{miss}}$, p_{T} of the leptons and the p_{T}-leading b-jet, jet multiplicity and b-jet multiplicity obtained with single-muon triggers.

6.4. Combined Background Validation

The agreement of data and MC samples for all background processes is studied for both the electron and the muon channel in a region as close to the signal region as possible. Therefore, the event selection of the preselection region is applied with an additional requirement on the dilepton invariant mass $M(\ell\ell) < 500\,\mathrm{GeV}$ to avoid signal contamination.
The composition of the combined background validation region for the electron and the muon channel is shown in Figure 6.8 and Figure 6.9 respectively. The event composition and event yields are similar for both channels, with the exception of the multijet background not being considered for the muon channel (cf. Section 6.2). The $t\bar{t}$ process dominates with a contribution of roughly 80%, followed by the Z$\ell\ell$ processes with a contribution of roughly 10%.
The dilepton invariant mass spectrum, $E_{\mathrm{T}}^{\mathrm{miss}}$ distribution and b-jet multiplicity of the electron and muon channel are presented in Figure 6.10. All variables show a good agreement between the data and MC event yields and a similar behaviour as seen in the top control region. The statistical uncertainties increase in the high $E_{\mathrm{T}}^{\mathrm{miss}}$ region and most events are reconstructed with one b-jet, although a significant fraction of $t\bar{t}$ events is reconstructed with two b-jets.
Additional kinematic variables and angular distributions for both channels are presented in Figure A.4, all of which show a good agreement between data and MC samples as well. It can therefore be concluded that the combined background validation region is well modelled for both channels.

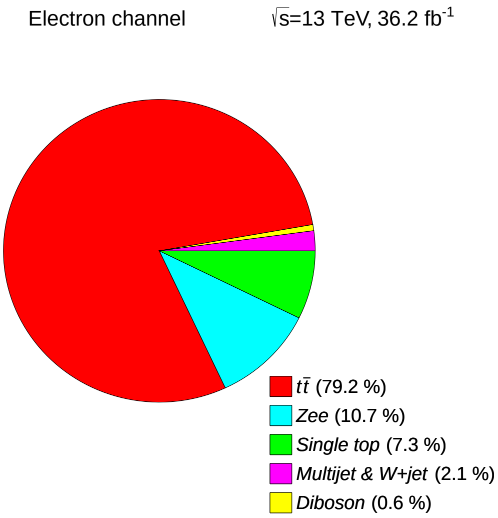

Figure 6.8.: Composition of the combined background validation region for the electron channel.

Table 6.6.: Event yields per process for the electron channel.

Process	Event Yield
Diboson	101
Multijet	336
Single top	1151
Zee	1691
$\mathrm{t\bar{t}}$	12480
Total	15760
Data	15910

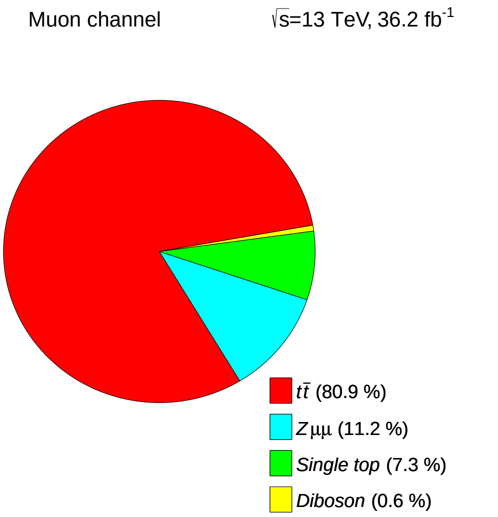

Figure 6.9.: Composition of the combined background validation region for the muon channel.

Table 6.7.: Event yields per process for the muon channel.

Process	Event Yield
Diboson	82
Single top	981
$Z\mu\mu$	1496
$\mathrm{t\bar{t}}$	10810
Total	13370
Data	13450

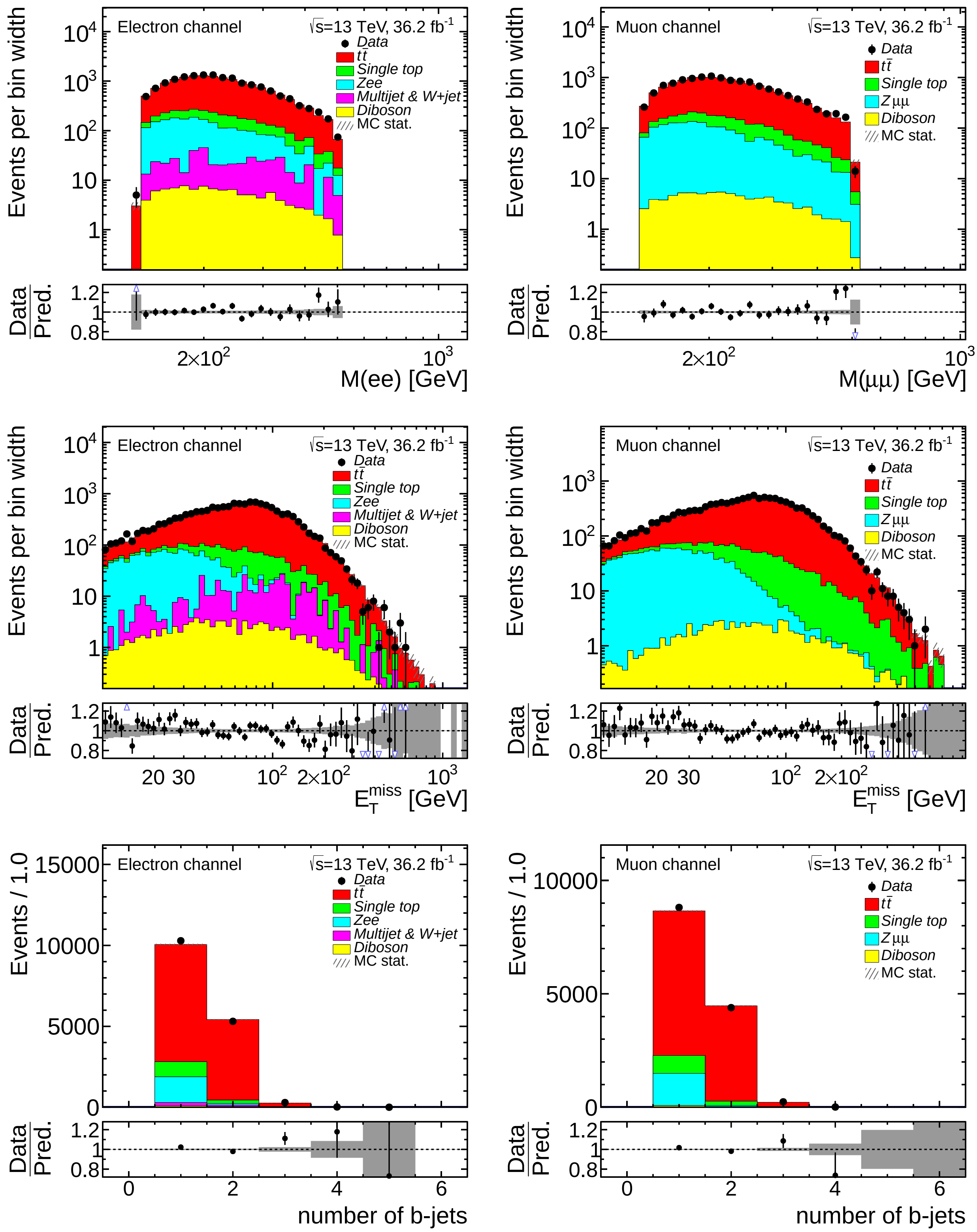

Figure 6.10.: Dilepton invariant mass, $E_{\mathrm{T}}^{\mathrm{miss}}$ and b-jet multiplicity of the electron channel (left) and muon channel (right).

7. Signal Samples

A closer look at the produced signal samples is presented in this chapter. A comparison of Z' signal samples produced with different detector simulation programmes is presented in Section 7.1, and event kinematics of the signal processes are discussed in Section 7.2. Starting out from the preselection region, two different approaches for defining a signal region are discussed in Section 7.3, relying solely on the discriminating power of the $\sigma(E_{\mathrm{T}}^{\mathrm{miss}})$ and optimizing the event selection with a neural network (NN) respectively.

7.1. Comparison of FullSim and Atlfast II

The detector simulation of the Z' signal samples is done with Atlfast II to reduce computation time (cf. Section 4.2). In order to check whether the high-mass region of the reconstructed dilepton system is well modelled, additional Z'$\ell\ell$ signal samples are produced with FullSim for a Z' mass of 1 TeV for a comparison between the two simulations. The comparison is done for both the muon and the electron channel in the respective preselection region (cf. Table 6.1).

Figure 7.1 shows the invariant mass distributions for the electron channel and the muon channel. The steep rise of the event fraction seen in the electron channel at roughly 600 GeV is caused by the event generator MadGraph, where a cutoff parameter on the invariant mass of the Z' at truth level is introduced. For the muon channel, the cutoff cannot be seen as clearly, as the lower momentum resolution of muons with high p_{T} results in a higher fraction of dimuon systems being reconstructed with an invariant mass below the generator level cutoff.

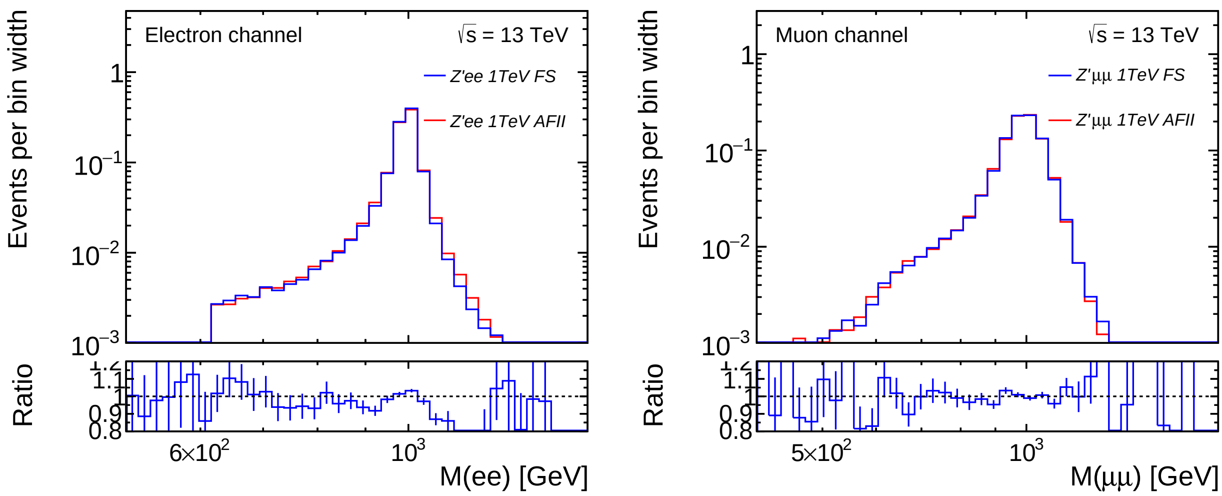

Figure 7.1.: Invariant mass distribution of the electron channel (left) and muon channel (right).

In the electron channel, a slight difference between Atlfast II and FullSim can be seen in the high-mass tail, but for the peak of the distribution the simulations agree well, and in the muon channel there is no deviation to be seen. For other variables, such as the transverse momenta of the leptons and the b-jet, the $E_{\mathrm{T}}^{\mathrm{miss}}$ and the jet multiplicity, the Atlfast II and FullSim samples show a very good agreement in both channels (cf. Appendix A.3). Therefore, it can be concluded that the signal samples simulated with Atlfast II can be used for the analysis, as no significant deviations from the FullSim samples were observed.

7.2. Kinematic distributions

MC samples of the Z' signal process are produced for Z' masses of 0.5 TeV, 1 TeV and 2 TeV for both the electron and the muon channel with all signal samples consisting of $2 \cdot 10^5$ generated events. The number of MC generated events remaining in the preselection region (cf. Table 6.1) per sample are listed in Table 7.1. For the muon channel, about 50% of the generated events do not pass the selection criterion of exactly two signal muons, leading to fewer events passing the selection in comparison to the electron channel. The `HighPtCaloOnly` isolation criterion applied for the electron channel results in fewer accepted events for the 0.5 TeV sample in comparison to the samples for higher masses, as the fraction of electrons passing the criterion exhibits a minimum for electrons with $p_{\mathrm{T}} \approx 230$ GeV (cf. Section 6.2.2). Cutflows for all signal samples, documenting how many event pass the individual event selection criteria, can be found in Table A.2 and Table A.3.

The dilepton invariant mass distributions for both channels are presented in Figure 7.2. The samples are generated with a relative Z' width of 4.6% [42], resulting in the total width increasing with the Z' mass. As discussed in Section 7.1, the cutoff on the Z' mass introduced by MadGraph is well visible in the electron channel. For the muon channel, the low-mass tail of the dilepton invariant mass distribution becomes more pronounced for higher Z' masses as the momentum resolution decreases with increasing p_{T}.
This effect can also be seen in the distribution of $E_{\mathrm{T}}^{\mathrm{miss}}$ and the difference in p_{T} between the truth level leptons ℓ^{truth} and the reconstructed leptons ℓ^{reco}, all of which are presented in Figure 7.3. The $E_{\mathrm{T}}^{\mathrm{miss}}$ as well as the Δp_{T} distributions stay relatively constant in the electron channel but increase with the Z' mass in the muon channel. In the electron channel, most events are collected in the first bin of the Δp_{T} distributions. In the muon channel, the Δp_{T} distributions show an increasing fraction of events with a high Δp_{T} for increasing Z' masses.

Table 7.1.: Number of MC events of the Z' signal samples in the preselection region.

Z' Mass	$Z' \to ee$	$Z' \to \mu\mu$
0.5 TeV	78504	63797
1 TeV	84213	64998
2 TeV	90081	63957

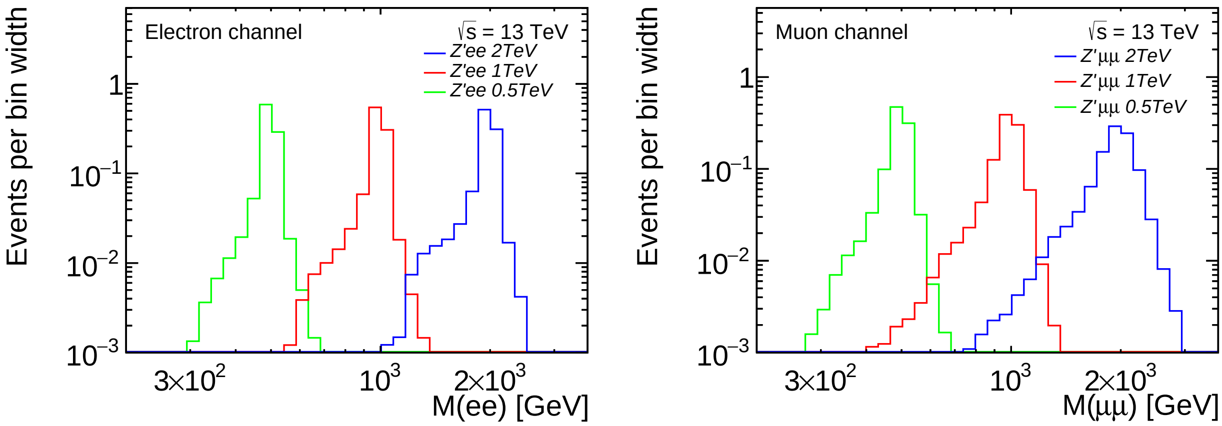

Figure 7.2.: Dilepton invariant mass of the Z' signal samples for the electron channel (left) and muon channel (right).

The angular distance between $E_{\mathrm{T}}^{\mathrm{miss}}$ and the leptons and the angular distance between $E_{\mathrm{T}}^{\mathrm{miss}}$ and the p_{T}-leading b-jet are presented in Figure 7.4. The structure of the $\Delta\phi(\mu_1, E_{\mathrm{T}}^{\mathrm{miss}})$ distribution peaking at $\pm\pi$ and the $\Delta\phi(\mu_2, E_{\mathrm{T}}^{\mathrm{miss}})$ distribution peaking at zero becomes more pronounced with increasing Z' masses. This shows how the $E_{\mathrm{T}}^{\mathrm{miss}}$ is mostly measured in the direction of flight of the p_{T}-subleading muon, opposite to the direction of flight of the p_{T}-leading muon as the muons are emitted back-to-back in order to conserve the momentum of the Z'.
The $\Delta\phi(b\text{-jet}_1, E_{\mathrm{T}}^{\mathrm{miss}})$ distribution also exhibits a peak at zero, as neutrinos can be produced in semi-leptonic decays of b-hadrons. The peak structure is more pronounced in the electron channel. For the muon channel, the peak around zero exhibits a broader distribution and becomes less pronounced for increasing Z' masses in accordance with the behaviour seen in the other variables discussed above.

The p_{T} and rapidity Y of the reconstructed Z' as well as the η of the p_{T}-leading b-jet are presented in Figure 7.5. For both channels, the effects of the increasing Z' mass can be seen very clearly, with a higher Z' mass resulting in a higher p_{T} of the Z' and the b-jet being emitted in a more forward direction, as the Z' is predominantly produced with a rapidity close to zero.
Overall, the generated Z' signal samples provide sufficient event statistics for further analysis and exhibit the expected behaviour for all discussed variables.

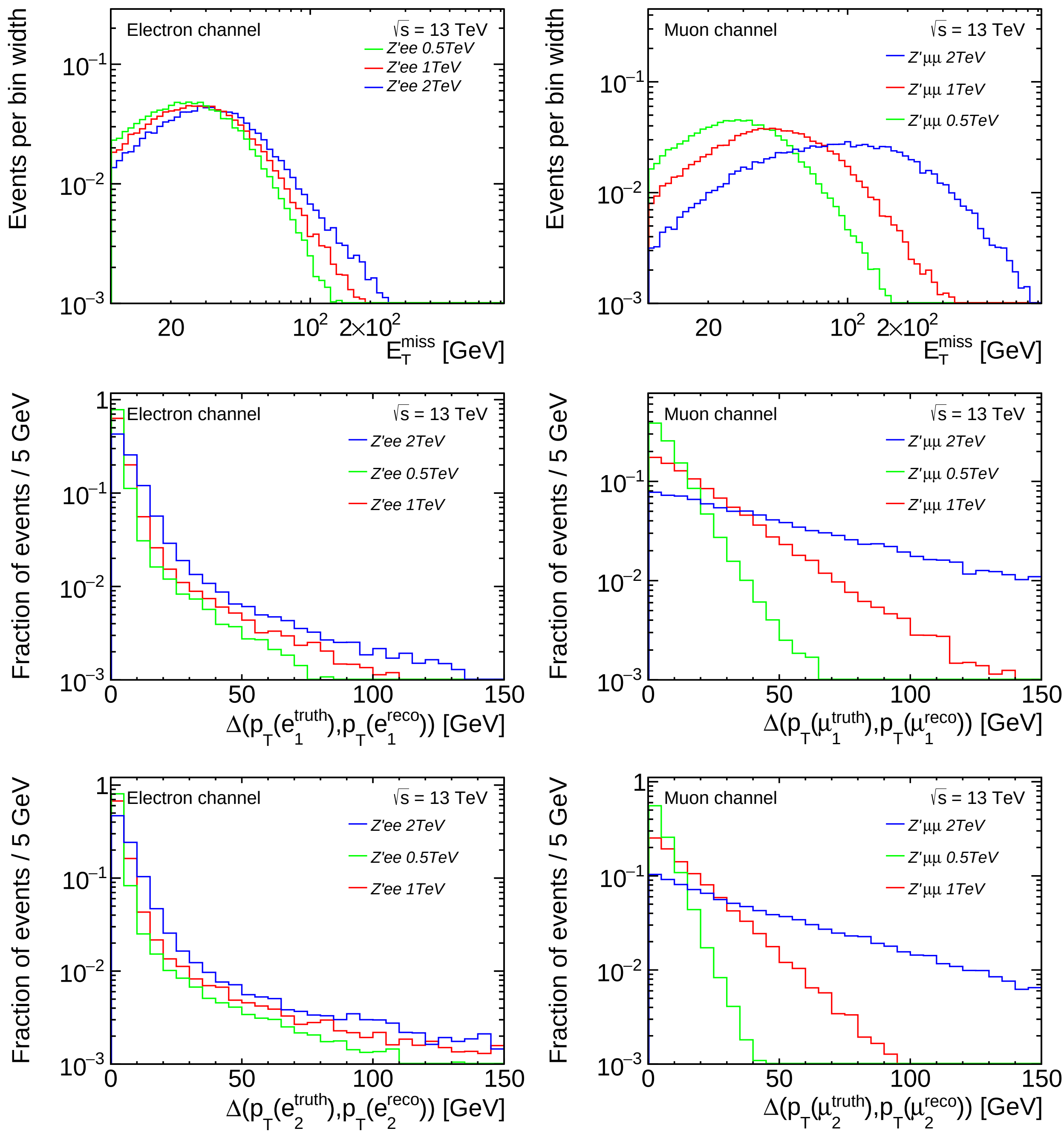

Figure 7.3.: $E_{\mathrm{T}}^{\mathrm{miss}}$ and the difference between the lepton p_{T} on truth level $p_{\mathrm{T}}(\ell^{\mathrm{truth}})$ and after detector reconstruction $p_{\mathrm{T}}(\ell^{\mathrm{reco}})$ for the electron channel (left) and muon channel (right).

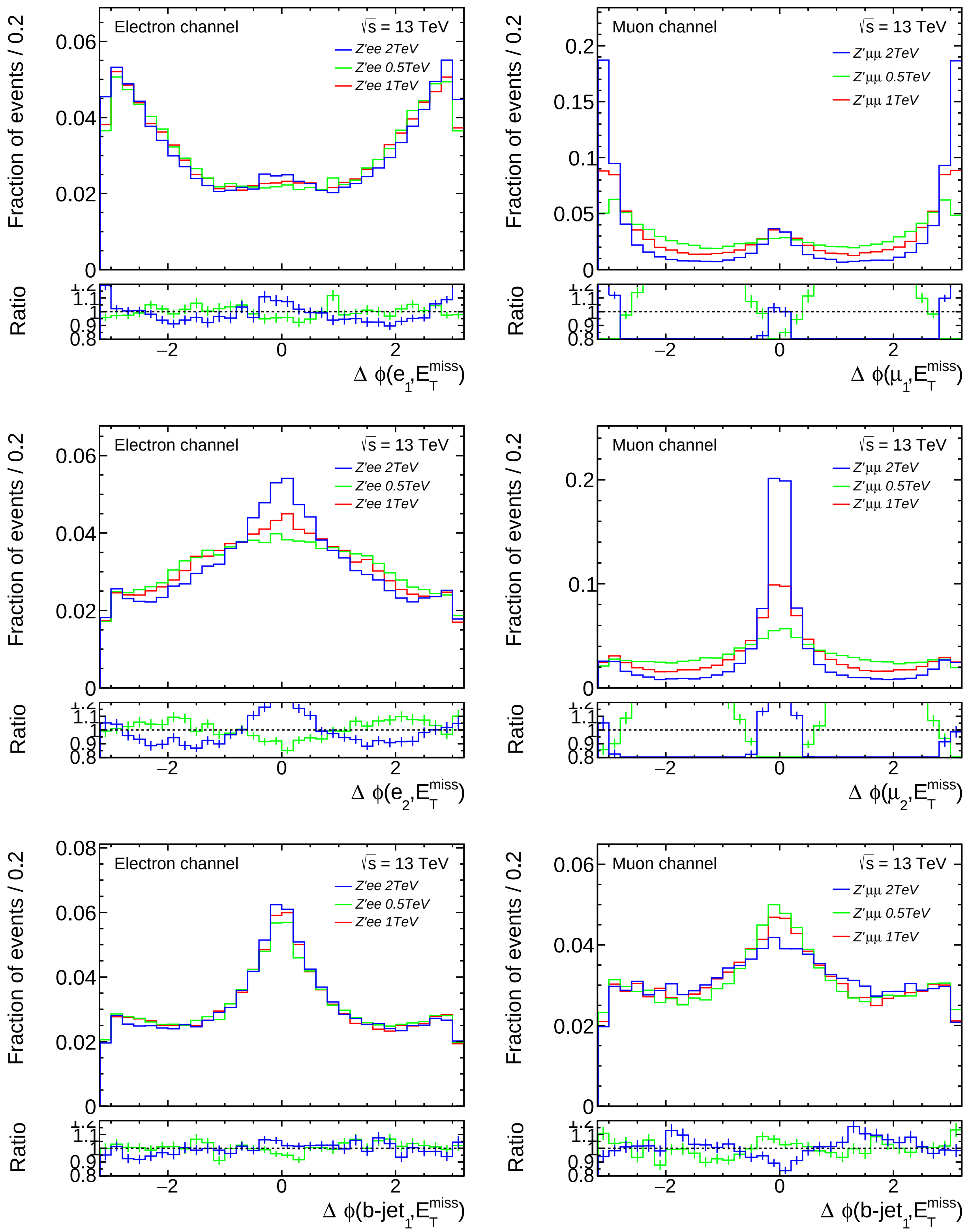

Figure 7.4.: Distance in ϕ between $E_{\mathrm{T}}^{\mathrm{miss}}$ and the p_{T}-leading lepton, the p_{T}-subleading lepton and the p_{T}-leading b-jet for the electron channel (left) and muon channel (right).

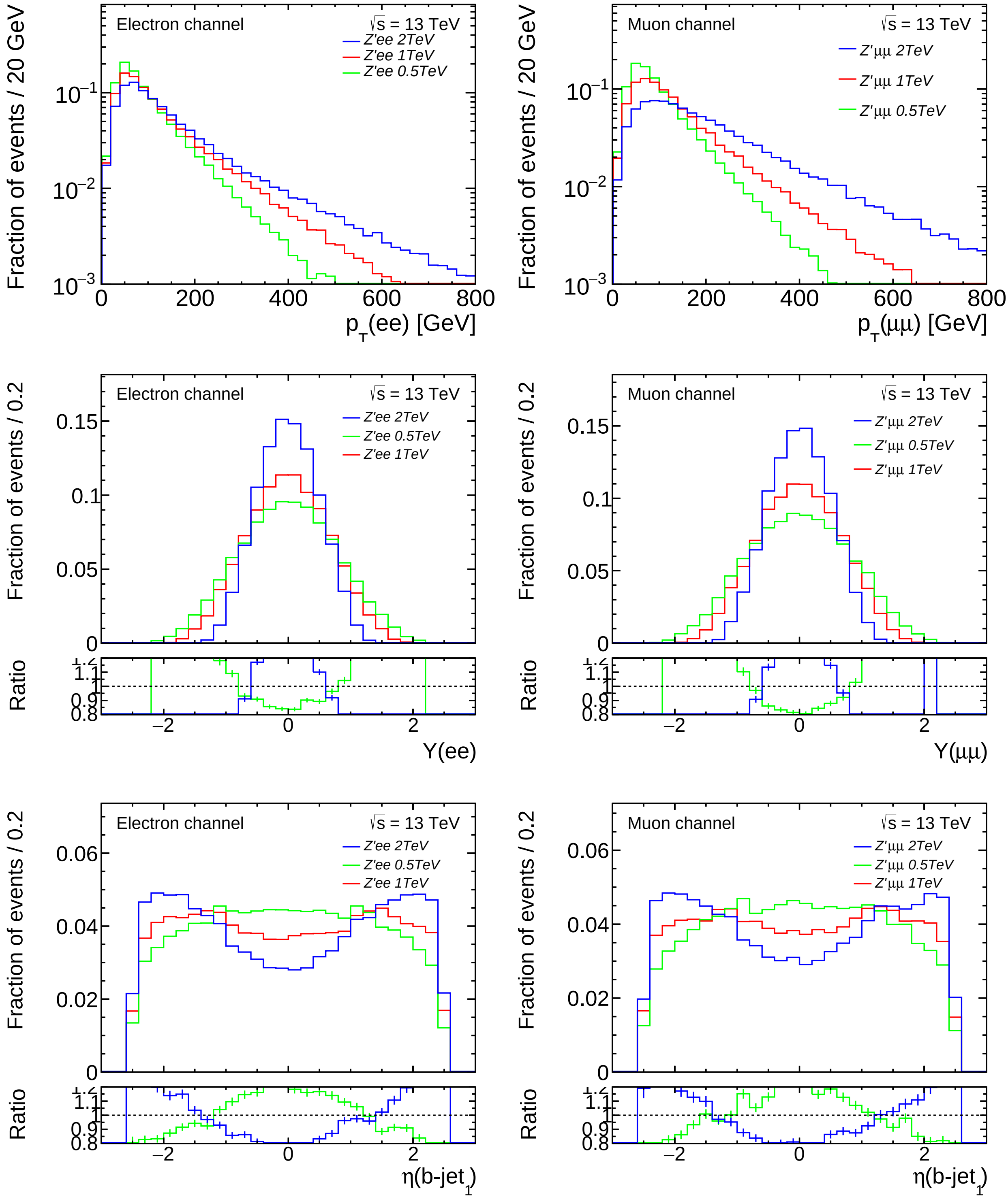

Figure 7.5.: p_{T} of the reconstructed Z' and η of the p_{T}-leading b-jet for the electron channel (left) and muon channel (right).

7.3. Signal and Background Separation

The dilepton invariant mass spectra of the signal and background processes for the electron and muon channel can be found in Figure 7.6 and Figure 7.7 respectively. For both channels, the expected event yield for the highest Z' mass of 2 TeV is very low with roughly one expected event. The lower Z' masses however exhibit considerably higher expected event yields, producing visible peaks in the invariant mass spectra.

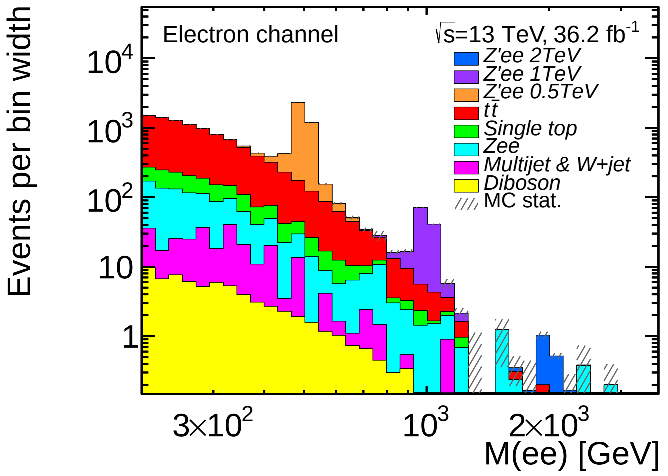

Figure 7.6.: Dielectron invariant mass spectrum in the preselection region.

Table 7.2.: Event yields per process for the electron channel.

Process	Event Yield
Diboson	108
Multijet	342
Single top	1190
Zee	1745
$t\bar{t}$	12800
$Z'ee$ 0.5 TeV	3634
$Z'ee$ 1 TeV	119
$Z'ee$ 2 TeV	1.6

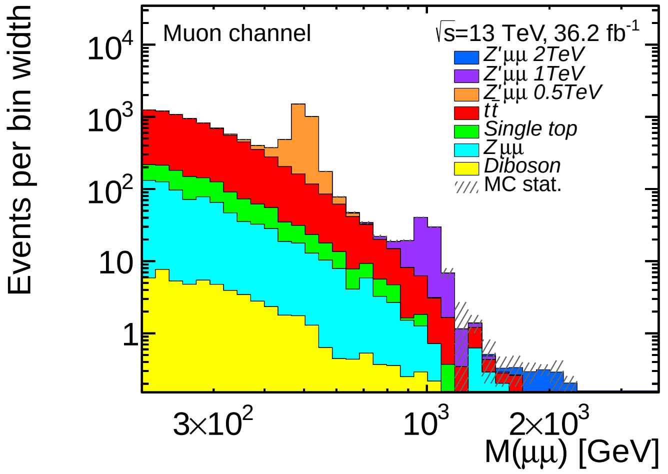

Figure 7.7.: Dimuon invariant mass spectrum in the preselection region.

Table 7.3.: Event yields per process for the muon channel.

Process	Event Yield
Diboson	87
Single top	1017
$Z\mu\mu$	1544
$t\bar{t}$	11123
$Z'\mu\mu$ 0.5 TeV	2830
$Z'\mu\mu$ 1 TeV	88
$Z'\mu\mu$ 2 TeV	1.1

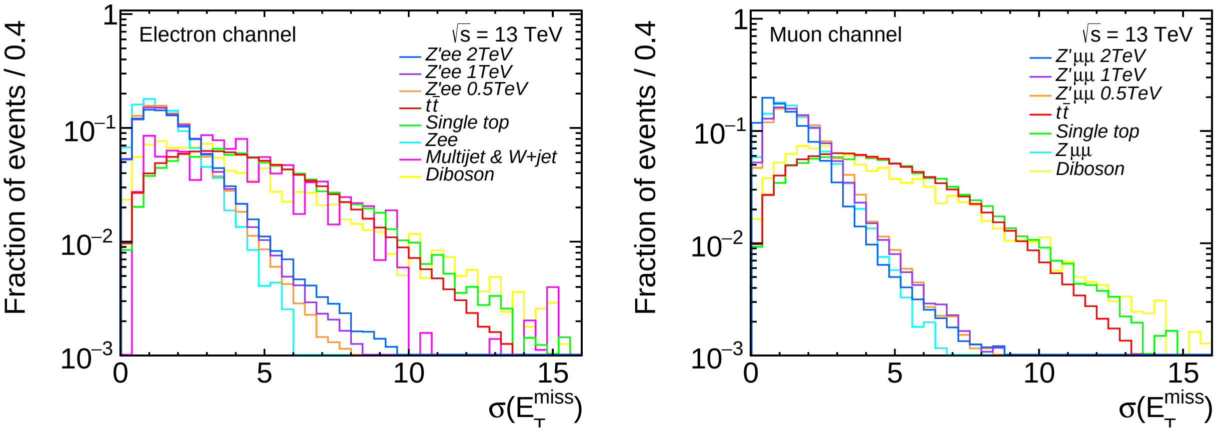

Figure 7.8.: $\sigma(E_{\mathrm{T}}^{\mathrm{miss}})$ of signal and background processes for the electron channel (left) and muon channel (right).

In order to reduce the contribution of background events further, an additional event selection requirement based on the $E_{\mathrm{T}}^{\mathrm{miss}}$ significance is introduced. The $\sigma(E_{\mathrm{T}}^{\mathrm{miss}})$ is used to distinguish between events with $E_{\mathrm{T}}^{\mathrm{miss}}$ originating from neutrinos and $E_{\mathrm{T}}^{\mathrm{miss}}$ originating from measurement uncertainties (cf. Chapter 5). The $E_{\mathrm{T}}^{\mathrm{miss}}$ of the $t\bar{t}$ process, being the largest background process, originates from neutrinos whereas the $E_{\mathrm{T}}^{\mathrm{miss}}$ of the signal processes is caused by limited momentum resolutions. Therefore, the $\sigma(E_{\mathrm{T}}^{\mathrm{miss}})$ provides a good opportunity for background reduction.

The $\sigma(E_{\mathrm{T}}^{\mathrm{miss}})$ distributions normalized to unity for the electron and muon channel are presented in Figure 7.8. An event selection requirement of $\sigma(E_{\mathrm{T}}^{\mathrm{miss}}) < 4.0$ is chosen to keep the loss of signal events around 1%. The invariant mass spectra obtained with the additional criterion for the electron and muon channel are presented in Figure 7.9 and Figure 7.9 respectively. It can be seen that the event yield of the signal processes remains almost unchanged, meaning that the $\sigma(E_{\mathrm{T}}^{\mathrm{miss}})$ requirement is especially suitable for the Z' mass of 2 TeV where no further reduction of the signal event yield can be tolerated. At the same time, the event yield of the $t\bar{t}$ process decreases by roughly 50% in both channels, proving the $\sigma(E_{\mathrm{T}}^{\mathrm{miss}})$ requirement to provide an effective background reduction.

As a second approach to reduce the contribution of background events, the event selection of the preselection region is optimized with an NN.

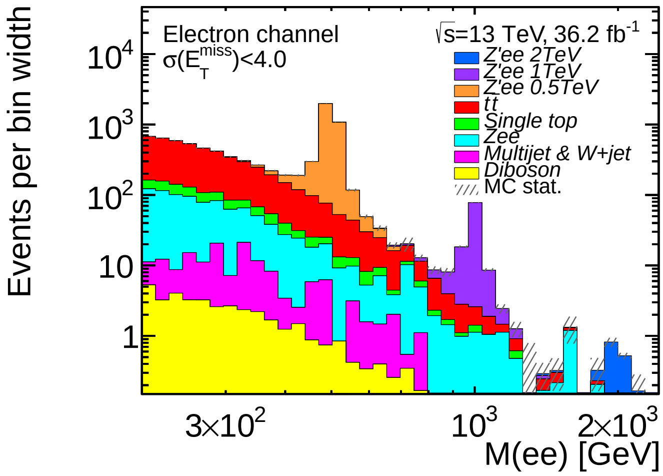

Figure 7.9.: Dielectron invariant mass spectrum with an additional requirement on $\sigma(E_{\mathrm{T}}^{\mathrm{miss}}) < 4.0$.

Table 7.4.: Event yields per process for the electron channel.

Process	Event Yield
Diboson	64
Multijet	187
Single top	543
Zee	1681
$t\bar{t}$	6242
Z'ee 0.5 TeV	3410
Z'ee 1 TeV	110
Z'ee 2 TeV	1.5

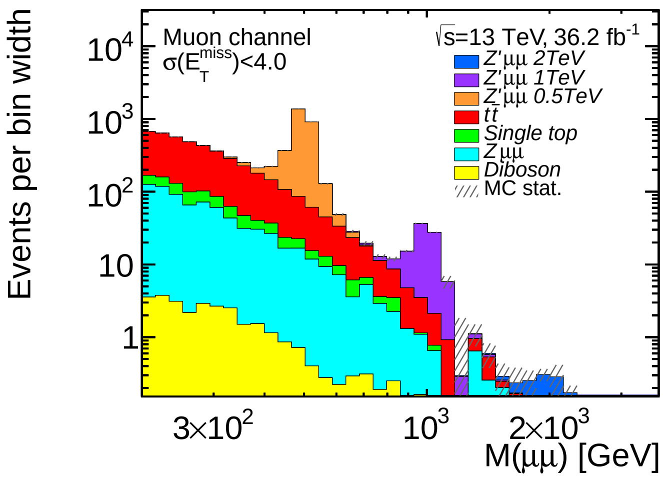

Figure 7.10.: Dimuon invariant mass spectrum with an additional requirement on $\sigma(E_{\mathrm{T}}^{\mathrm{miss}}) < 4.0$.

Table 7.5.: Event yields per process for the muon channel.

Process	Event Yield
Diboson	48
Single top	469
$Z\mu\mu$	1486
$t\bar{t}$	5471
Z'$\mu\mu$ 0.5 TeV	2654
Z'$\mu\mu$ 1 TeV	82
Z'$\mu\mu$ 2 TeV	1.0

7.3.1. Neural Network

NNs are computing systems modelled after the human brain, consisting of multiple layers of computing nodes processing the input data, and suitable for a variety of different tasks [43]. One usage of NNs is the classification of input data according to given categories, meaning that an NN can be trained to discriminate between signal and background events. As NNs are sensitive to correlations between input variables and take them into account for the classification of events, a better discrimination between signal and background events is expected in comparison to an event selection optimized by a sole requirement of $\sigma(E_{\mathrm{T}}^{\mathrm{miss}}) < 4.0$.

The NeuroBayes® package [44, 45], originally developed as a tool for high energy physics, is used for the presented analysis. The NN consists of three layers, an input layer with one node per input variable and an additional bias node, a hidden layer with a number of nodes as specified by the user and the output layer with only one output node. The input I_j of a node j is given by the linear sum of the output values x_i of all nodes in the previous layer multiplied with a weight w_{ij} respectively

$$I_j = \sum_i w_{ij} x_i. \tag{7.1}$$

The output of every node is mapped on the interval [-1,1] before being fed to the nodes of the following layer by applying the sigmoid function

$$S(x) = \frac{2}{1 + e^{-x}} - 1. \tag{7.2}$$

During the training of the NN, the weights w_{ij} are optimized in an iterative process by minimizing the entropy loss function, which is a measure for the goodness of the signal and background separation reached by the NN. The output value of the single output node is linearly mapped on the interval [0,1], with a high value of this so-called NNout distribution corresponding to a high probability for the event being a signal event.

The NN is trained on the MC events of the preselection region, with 80% of the events being used in the training and 20% being used for testing the NN in order to prevent overtraining. An event weighting is applied to train on a dataset consisting of 50% signal and 50% background events.
A preprocessing procedure is applied to the input variables to allow for the usage of any variable deemed useful from a physical perspective without being hindered by technical constraints. As a first step, for each input variable the sum of signal and background events is transformed to a flat distribution consisting of 100 bins. A purity distribution, defined as the fraction of signal events per bin, is then calculated and fitted with a spline function to reduce statistical fluctuations. The resulting distributions are again transformed into Gaussian distributions with a mean value of zero and a width of one. For each variable, the correlation with every other input variable as well as with the target is calculated. The significance of every variable is determined by calculating the correlation loss caused by removing the respective variable. Only variables with a significance of at least 3σ are used to train the NN. As a final step before the training, the input variables are decorrelated from each other. For integer input variables, a different preprocessing is applied, whith regularised mean values for an unordered class being used instead of a spline fit.

Only the largest background processes, $t\bar{t}$, single top and $Z\ell\ell$, are included in the training. The dilepton invariant mass and p_{T} distributions are not used as input variables to avoid the NN discriminating between signal and background events mainly according to the Z' mass, as the NN would become insensitive to lower Z' masses by construction. Instead, angular

distributions of and angular differences between the reconstructed objects are used as well as the jet multiplicity, $E_{\mathrm{T}}^{\mathrm{miss}}$ and $\sigma(E_{\mathrm{T}}^{\mathrm{miss}})$.
The network is trained separately for each Z' signal sample. The significance ranking of the input variables found for each signal process is presented in Table 7.6, with a grey background indicating a significance below 3σ. It can be seen how the $E_{\mathrm{T}}^{\mathrm{miss}}$ is found to be more important for the muon channel than for the electron channel as well as the $\sigma(E_{\mathrm{T}}^{\mathrm{miss}})$, being the most important variable for the two highest Z' masses in the muon channel while being ranked lower with increasing Z' masses in the electron channel. The η distributions of single particles are generally ranked low, whereas the rapidity of the reconstructed dilepton system gains importance with increasing Z' masses for both lepton channels.
The NNout distributions obtained for the Z'$\ell\ell$ samples for a Z' mass of 0.5 TeV are presented in Figure 7.11. The separation between signal and background events is very good for both channels with most $t\bar{t}$ and single top events being classified with small NNout values and most signal events being classified with values above 0.8. The NNout distributions for the other signal samples, all showing a similar behaviour, are presented in Figure A.7.
According to the results of the NN training, an event selection requirement of NNout > 0.8 is introduced. The event yields of the background and signal processes obtained in the preselection region in comparison to the event yields obtained with the additional NNout requirement are presented in Table 7.7. It can be seen how the event yield of the background processes is reduced by more than 90% for all signal samples. The signal event yield is decreased by about 30% for the Z' mass of 0.5 TeV, with the reduction decreasing to roughly 20% for the samples with a Z' mass of 2 TeV. The signal over background ratio greatly increases for all signal samples, with the signal region even containing more signal than background events in both lepton channels for the lowest Z' mass.

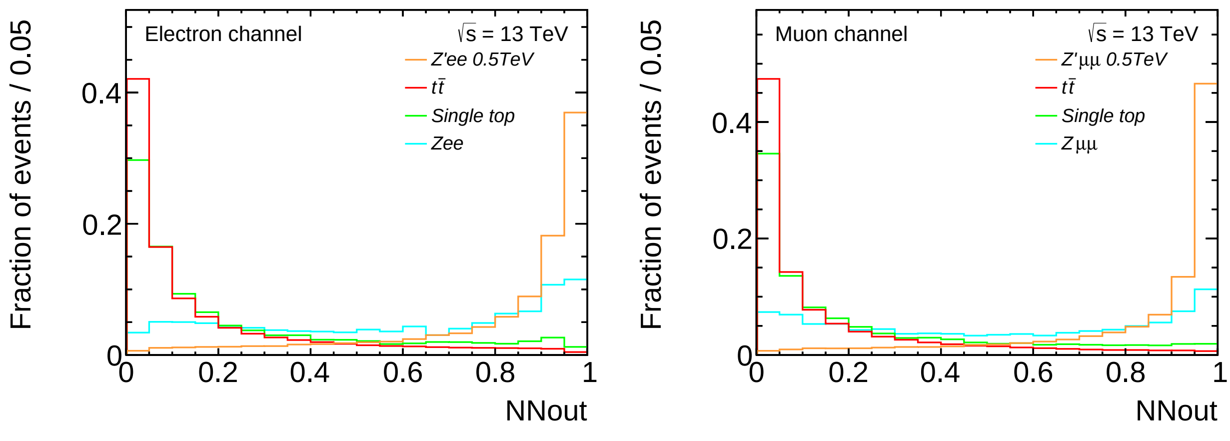

Figure 7.11.: NNout distributions obtained for the Z'$\ell\ell$ signal samples with a Z' mass of 0.5 TeV for the electron channel (left) and for the muon channel (right).

Overall, it can be concluded that the background reduction with an NN based on the chosen input variables works well, with the significance of the individual variables depending on the considered lepton channel as well as on the Z' mass. In comparison to the signal selection with an $\sigma(E_{\mathrm{T}}^{\mathrm{miss}}) < 4.0$ requirement, for which a table containing the event yields of signal and background processes is presented in Table A.4, the number of background events in the signal region is reduced more strongly. Although the number of signal events is reduced as well, the signal-over-background ratio reached with the NN is better by up to a factor of ten compared to the event selection based on $\sigma(E_{\mathrm{T}}^{\mathrm{miss}})$.

Table 7.6.: Ranking of the variables used by the NN for the Z'$\ell\ell$ signal processes. Variables with a significance of less than 3σ are highlighted in grey.

Ranking	Z'ee 0.5 TeV	Z'ee 1 TeV	Z'ee 2 TeV	Z'$\mu\mu$ 0.5 TeV	Z'$\mu\mu$ 1 TeV	Z'$\mu\mu$ 2 TeV
1	# jets	$\Delta\phi(ee, b\text{-jet}_1)$	$\Delta R(e_1, e_2)$	# jets	$\sigma(E_{\mathrm{T}}^{\mathrm{miss}})$	$\sigma(E_{\mathrm{T}}^{\mathrm{miss}})$
2	$\sigma(E_{\mathrm{T}}^{\mathrm{miss}})$	$\Delta R(e_1, e_2)$	$\Delta\phi(ee, b\text{-jet}_1)$	$\sigma(E_{\mathrm{T}}^{\mathrm{miss}})$	# jets	$\Delta R(\mu_1, \mu_2)$
3	$\Delta\phi(ee, b\text{-jet}_1)$	$\sigma(E_{\mathrm{T}}^{\mathrm{miss}})$	$\Delta y(ee, b\text{-jet}_1)$	$\Delta\phi(\mu\mu, b\text{-jet}_1)$	$E_{\mathrm{T}}^{\mathrm{miss}}$	$E_{\mathrm{T}}^{\mathrm{miss}}$
4	$\Delta y(ee, b\text{-jet}_1)$	# jets	$\sigma(E_{\mathrm{T}}^{\mathrm{miss}})$	$\Delta y(\mu\mu, b\text{-jet}_1)$	$\Delta R(\mu_1, \mu_2)$	# jets
5	$\Delta R(e_1, e_2)$	$\Delta y(ee, b\text{-jet}_1)$	$y(ee)$	$\Delta R(\mu_1, \mu_2)$	$\Delta\phi(\mu\mu, b\text{-jet}_1)$	$y(\mu\mu)$
6	$\Delta\phi(b\text{-jet}_1, E_{\mathrm{T}}^{\mathrm{miss}})$	$\Delta\phi(b\text{-jet}_1, E_{\mathrm{T}}^{\mathrm{miss}})$	# jets	$\Delta\phi(\mu_1, E_{\mathrm{T}}^{\mathrm{miss}})$	$\Delta y(\mu\mu, b\text{-jet}_1)$	$\Delta\phi(\mu_1, E_{\mathrm{T}}^{\mathrm{miss}})$
7	$y(ee)$	$y(ee)$	$\Delta\phi(b\text{-jet}_1, E_{\mathrm{T}}^{\mathrm{miss}})$	$E_{\mathrm{T}}^{\mathrm{miss}}$	$y(\mu\mu)$	$\Delta y(\mu\mu, b\text{-jet}_1)$
8	$E_{\mathrm{T}}^{\mathrm{miss}}$	$\eta(e_1)$	$E_{\mathrm{T}}^{\mathrm{miss}}$	$\Delta\phi(b\text{-jet}_1, E_{\mathrm{T}}^{\mathrm{miss}})$	$\Delta\phi(b\text{-jet}_1, E_{\mathrm{T}}^{\mathrm{miss}})$	$\Delta\phi(\mu\mu, b\text{-jet}_1)$
9	$\Delta\phi(e_1, E_{\mathrm{T}}^{\mathrm{miss}})$	$\Delta\phi(e_1, E_{\mathrm{T}}^{\mathrm{miss}})$	$\eta(b\text{-jet}_1)$	$y(\mu\mu)$	$\Delta\phi(\mu_2, E_{\mathrm{T}}^{\mathrm{miss}})$	$\Delta\phi(\mu_2, E_{\mathrm{T}}^{\mathrm{miss}})$
10	$\eta(e_1)$	$E_{\mathrm{T}}^{\mathrm{miss}}$	$\eta(e_1)$	$\eta(\mu_1)$	$\eta(b\text{-jet}_1)$	$\Delta\phi(b\text{-jet}_1, E_{\mathrm{T}}^{\mathrm{miss}})$
11	$\Delta\phi(e_2, E_{\mathrm{T}}^{\mathrm{miss}})$	$\eta(e_2)$	$\eta(e_2)$	$\Delta\phi(\mu_2, E_{\mathrm{T}}^{\mathrm{miss}})$	$\Delta\phi(\mu_1, E_{\mathrm{T}}^{\mathrm{miss}})$	$\eta(\mu_1)$
12	$\eta(b\text{-jet}_1)$	$\eta(b\text{-jet}_1)$	$\Delta\phi(e_2, E_{\mathrm{T}}^{\mathrm{miss}})$	$\eta(\mu_2)$	$\eta(\mu_1)$	$\eta(\mu_2)$
13	$\eta(e_1)$	$\Delta\phi(e_2, E_{\mathrm{T}}^{\mathrm{miss}})$	$\Delta\phi(e_1, E_{\mathrm{T}}^{\mathrm{miss}})$	$\eta(b\text{-jet}_1)$	$\eta(\mu_2)$	$\eta(b\text{-jet}_1)$

Table 7.7.: Event yields of background and signal events in the preselection region (presel.) and with an additional event selection requirement of NNout> 0.8 (NNout).

Signal sample	Background		Signal		Sover B [%]	
	presel.	NNout	presel.	NNout	presel.	NNout
Z'ee 0.5 TeV	15730	1150	3634	2540	23.1	221
Z'ee 1 TeV	15730	893	119	86	0.8	9.6
Z'ee 2 TeV	15730	713	1.6	1.27	0.01	0.2
Z'$\mu\mu$ 0.5 TeV	13680	868	2830	2030	20.7	234
Z'$\mu\mu$ 1 TeV	13680	524	88	72	0.6	13.7
Z'$\mu\mu$ 2 TeV	13680	604	1.1	0.94	0.008	0.16

8. Exclusion Limits

In the case that a search for new physics observes no signal excess in the data, exclusion limits on the considered model are set. In this chapter, a limit on the Z' production cross section is set for both lepton channels with the two signal region definitions described in the previous chapter. As the limit is determined from three mass points only without considering systematic uncertainties and without looking at data in the signal region, the obtained limits serve as a first estimation for the sensitivity to be expected from the full analysis.
The cross sections used for generating the Z' signal samples are recalculated for the setting of exclusion limits presented in the following. The coupling of the Z' to leptons of the respective channel's flavour is kept at the initial value, and the coupling to leptons of the other flavour is set to zero (cf. Section 4.2).
Section 8.1 provides an overview of the statistical method used to set limits on the signal strength. In Section 8.2, the binning of the dilepton invariant mass distribution used for the fitting is discussed, and the fitting procedure is explained in Section 8.3. The obtained limits on the Z' mass are presented in Section 8.4 and compared to the limits obtained in previous analyses in Section 8.5.

8.1. Statistical techniques

The exclusion limits are set with the CL_s technique [46] implemented in the `RooFit` toolkit [47]. The TRExFitter framework is used to perform a binned maximum-likelihood fit to test the compatibility of the signal hypothesis with the data [48]. The likelihood function used for the fit consists of a Poisson term for each bin i of the fitted distribution and an additional term for nuisance parameters (NPs) θ representing systematic uncertainties and the total number of background events:

$$L(\mu, \boldsymbol{\theta}) = \prod_{i=1}^{N} \frac{(\mu s_i + b_i)^{n_i}}{n_i!} \cdot e^{-(\mu s_i + b_i)} \prod_{j=1}^{M} \rho(\theta_j), \tag{8.1}$$

with s_i and b_i denoting the number of signal and background events per bin respectively and n_i being the total number of observed events per bin. The signal strength μ is a free parameter of the fit. The agreement between a hypothesized value for μ and the data is described by the profile likelihood ratio

$$\lambda(\mu) = \frac{L(\mu, \hat{\hat{\boldsymbol{\theta}}})}{L(\hat{\mu}, \hat{\boldsymbol{\theta}})}, \tag{8.2}$$

with $\hat{\hat{\boldsymbol{\theta}}}$ denoting the NPs maximizing the likelihood function for the considered μ and $L(\hat{\mu}, \hat{\boldsymbol{\theta}})$ being the maximized likelihood function.
The test statistic

$$t_\mu = -2\ln(\lambda(\mu)) \tag{8.3}$$

is used to quantify the level of agreement between the hypothesized μ_{obs} and the data by calculating the p-value

$$p_\mu = \int_{t_{\mu,obs}}^{\infty} f(t_\mu|\mu)dt_\mu, \tag{8.4}$$

with $f(t_\mu|\mu)$ denoting the probability density function of t_μ under the assumption of μ. The p-value can be used to set an upper limit on the signal strength by finding the μ for which p_μ equals 0.05. This corresponds to a confidence level (CL) of 95%, meaning that the obtained upper limit is equal to or larger than the true limit with a probability of 95%. In order to prevent exclusion of the signal due to statistical fluctuations of the background, the CL_s, defined as

$$CL_s = \frac{p_\mu}{1 - p_0} \tag{8.5}$$

is used for the limit setting, with p_0 being the p-value for the background-only hypothesis. A $\mathrm{CL}_s < 0.05$ corresponds to an exclusion of the signal with the considered μ at a CL of 95%.

8.2. Dilepton invariant mass resolution

The limit on the signal strength obtained in a fit depends on the binning of the fitted distribution, with a finer binning usually resulting in better limits. For the high invariant mass region, the choice of the bin widths is governed by the low event statistics. The invariant mass region below $\approx 650\,\mathrm{GeV}$ provides enough statistics for a finer binning, limited only by the detector resolution of the dilepton invariant mass.
In MC samples, the truth-level information describing a generated particle's properties before applying the detector simulation are accessible and can be used to study the detector resolution. To determine the resolution, a two-dimensional histogram of the truth invariant mass $M_{\mathrm{truth}}(\ell\ell)$ versus the reconstructed invariant mass $M_{\mathrm{reco}}(\ell\ell)$ is created. For each $M_{\mathrm{truth}}(\ell\ell)$ bin, a one-dimensional projection of the $M_{\mathrm{reco}}(\ell\ell)$ distribution is then created, with the RMS of this distribution being used as a measure for the resolution. A high RMS corresponds to a broad spreading of the $M_{\mathrm{reco}}(\ell\ell)$ values belonging to the same truth value. The $\mathrm{Z}\ell\ell$ MC samples are used to determine the $M(\ell\ell)$ resolution of the respective lepton channels. The event selection of the preselection region is applied (cf. Table 6.1) except for the b-tagging requirement, which is dropped in order to gain higher event statistics. The obtained dilepton invariant mass resolutions for the electron channel and the muon channel are presented in Figure 8.1. Both channels show a similar resolution, with the resolution of the muon channel being slightly better in the low invariant mass region. Therefore, the binning is chosen to stay above the resolution of the electron channel, as the same binning is used for both channels to keep the limit setting procedure consistent. In the dilepton invariant mass region above 620 GeV, broader bin widths are chosen to prevent bins with no background events. The following binning is chosen:

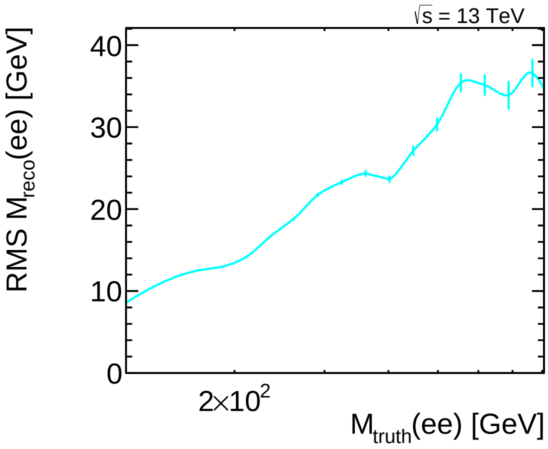

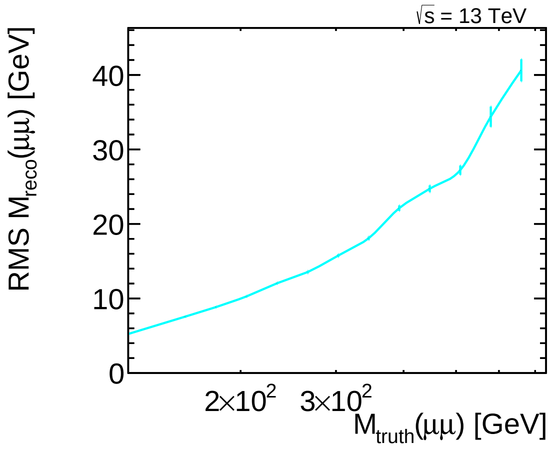

Figure 8.1.: Resolution of the dilepton invariant mass for the electron channel (left) and muon channel (right).

- bin width of 20 GeV from 130 GeV to 210 GeV
- bin width of 30 GeV from 210 GeV to 540 GeV
- bin width of 40 GeV from 540 GeV to 620 GeV
- one bin from 620 GeV to 720 GeV
- one bin from 720 GeV to 940 GeV
- one bin starting from 940 GeV

with the last bin collecting all events with an invariant mass above 940 GeV.

8.3. Fit procedure

As no systematic uncertainties are considered for the fit, the only NP is a normalisation factor (NF) μ_{ttbar} for the dominating background process, accounting for the difference between data and MC event yields. The NF is obtained from a background-only fit in the CR, meaning that the signal strength μ is set to zero for the fit. The top control region obtained with single-muon triggers (cf. Section 6.3.1) is used as CR, with real data being used for the fit. A NF of $\mu_{ttbar} = 0.97 \pm 0.01$ is obtained by fitting the dilepton invariant distribution of the CR summed up in one bin.
For the signal-plus-background fit performed to determine the limit on the signal strength, the SR and CR are fitted simultaneously. As no real data is used in the signal region, an Asimov dataset is created from the MC prediction for background event yields per bin, taking the normalisation factor obtained from the background-only fit in the CR into account to ensure consistency for the signal-plus-background fit.

An asymptotic limit on the signal strength is set, using the fact that the distribution of a test statistic t_μ of a sample is known to be parabolically shaped around the minimum [49], holding true for a sample size of the order of ten events $\mathcal{O}(10)$ or more.

8.4. Obtained Expected Limits

The limits on the signal strength obtained for the electron and muon channel in the two different signal regions are presented in Figure 8.2 and Figure 8.3 respectively. It can be seen that a slightly lower expected limit on the production cross section is obtained by the NN when compared to the $\sigma(E_{\mathrm{T}}^{\mathrm{miss}})$ selection for the lowest Z' mass of 0.5 TeV. For the higher masses, the difference between the obtained limits is reduced to less than 10%, resulting in a very similar result for the exclusion limit on the Z' mass of roughly 1.6 TeV. This can be explained by the broad binning chosen above 620 GeV due to the limited event statistics in the high dilepton invariant mass region. The Z' signal events for the Z' mass of 1 TeV are distributed in three bins only and for the highest Z' mass of 2 TeV, the signal event yield is completely collected within the last bin (cf. Figure A.8). As only a few background events remain in those bins even for the preselection region, the difference between the two signal event selections becomes almost negligible for the higher Z' masses.

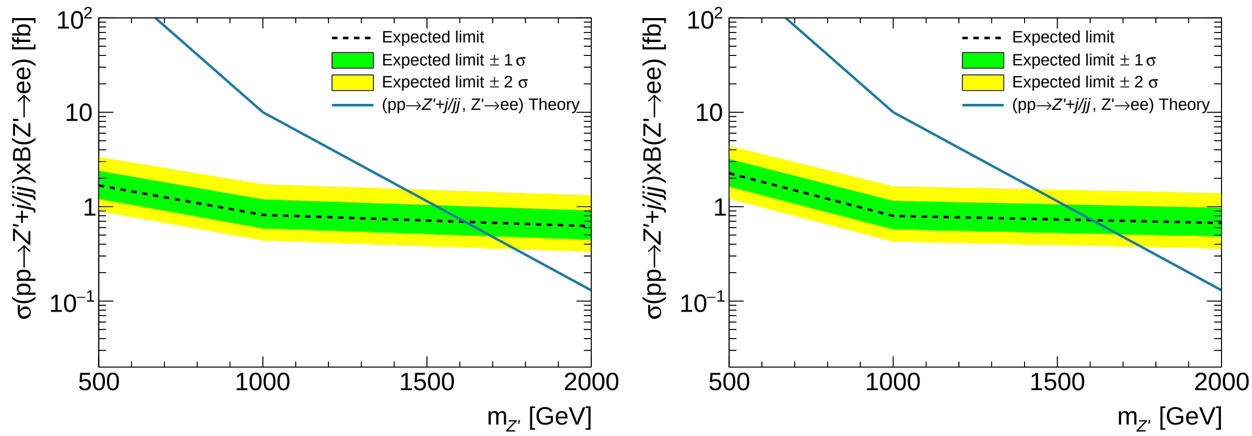

Figure 8.2.: Expected 95% CL upper limit on the cross section for the Z' production for the electron channel with a signal selection by NN (left) and by $\sigma(E_T^{miss}) < 4.0$ (right).

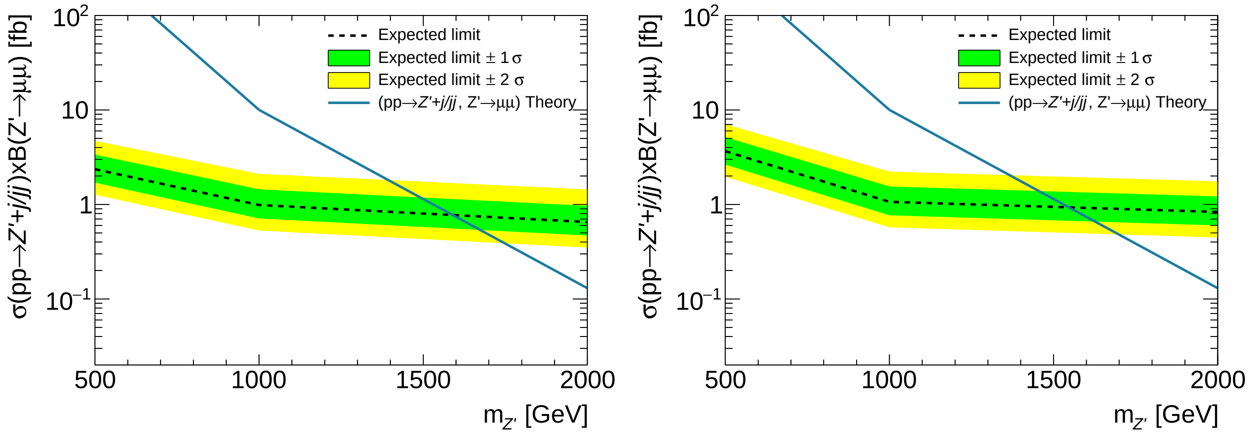

Figure 8.3.: Expected 95% CL upper limit on the cross section for the Z' production for the muon channel with a signal selection by NN (left) and by $\sigma(E_T^{miss}) < 4.0$ (right).

8.5. Comparison with inclusive limits

The limits obtained with the NN event selection are compared to the results of previous searches for dilepton resonances [50, 51], carried out with the 2015/16 dataset of $36.2\,\text{fb}^{-1}$ and the full Run 2 dataset of $139\,\text{fb}^{-1}$ respectively. As the searches were done for an inclusive Z' production, inclusive cross sections $\sigma(pp \rightarrow Z' + X) \times \mathcal{B}(Z' \rightarrow \ell\ell)$ for the Z' model used for this analysis are calculated with MadGraph. The Z' model used for the previous analysis allows couplings to first-generation quarks, therefore, the comparison is not straightforward but supposed to provide a rough estimate of how well the approach presented in this analysis performs compared to the inclusive search.
The Z' model used in this analysis has a relative width of 4.6%, therefore, the expected limits for a relative Z' width of 6.0% set in the inclusive analysis using the full Run 2 dataset are chosen for the comparison. The limit set in the inclusive analysis using the 2015/16 data was applied to different Z' models and extracted using a Z'$_{\text{SSM}}$ model with a relative width of 3% [50].
The inclusive cross section $\sigma(pp \rightarrow Z' + X) \times \mathcal{B}(Z' \rightarrow \ell\ell)$ of the Z' model used for this analysis and the expected limits obtained in the previous inclusive searches for both lepton channels are presented in Figure 8.4. It can be seen how the exclusion limit obtained with the 2015/16 dataset on the Z' mass is around 2.2 TeV for the electron channel and around 1.9 TeV for the muon channel, meaning that the limits set by the inclusive analysis are stronger than the limits obtained in this analysis.

As the binning of the invariant mass distribution in the signal region has a considerable impact on the obtained limits, the binning used by the inclusive analysis using the 2015/16 dataset is applied to the signal regions in order to study how much sensitivity can be gained. The binning is logarithmic with 48 bins in the interval [128 GeV, 3000 GeV]. The logarithmic binning results in very low event statistics per bin in the high invariant mass region (cf.

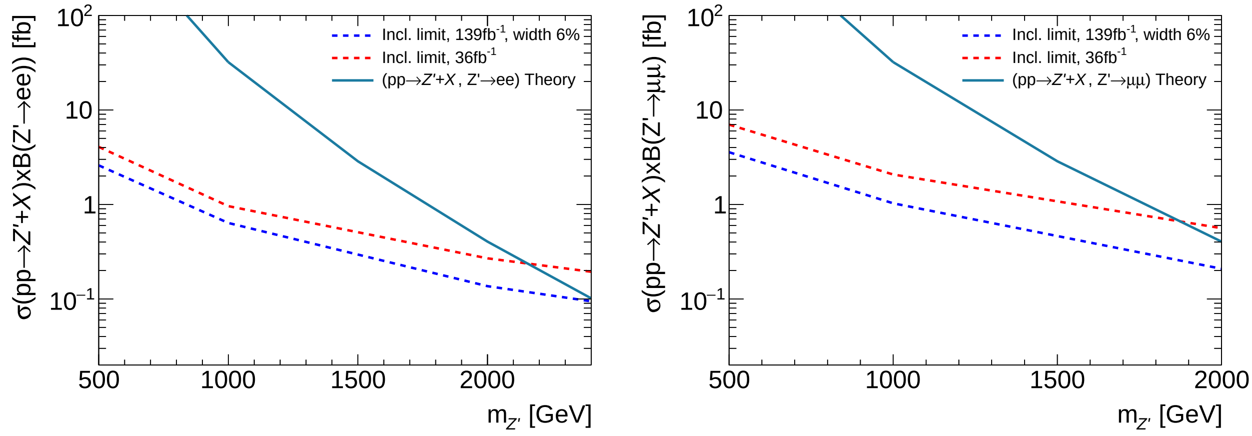

Figure 8.4.: Expected 95% CL upper limit on the inclusive cross section for the Z' production obtained in previous analyses [50, 51] for the electron channel (left) and muon channel (right). The theory curve represents the inclusive cross section of the Z' model considered in this analysis.

Figure A.9), meaning that even the usage of the full Run 2 dataset is not expected to reach ten events per bin. The asymptotic limit can therefore not be applied for a limit setting with the logarithmic binning when real data is used in the signal region.
The limits obtained for the electron and the muon channel using the logarithmic binning and the $\sigma(E_{\mathrm{T}}^{\mathrm{miss}})$ signal selection are presented in Figure A.10. The $\sigma(E_{\mathrm{T}}^{\mathrm{miss}})$ signal region is chosen for the comparison as the NN signal region contains less events, resulting in the fit procedure failing for the Z'*ee* signal sample for a Z' mass of 2 TeV. A comparison of the limits obtained in this analysis in the $\sigma(E_{\mathrm{T}}^{\mathrm{miss}})$ signal region with the logarithmic binning and the limits of the inclusive analysis using the 2015/16 data is presented in Figure 8.5.
It can be seen how the logarithmic binning results in considerably better limits on the Z' mass of 1.7 TeV for the muon channel and 1.8 TeV for the electron channel. A better limit is reached for the electron channel than for the muon channel analogously to the inclusive analyses. The obtained expected limits on the cross section are lower than the expected limits of the inclusive analysis, but the predicted cross section for an inclusive Z' production is considerably larger than the cross section for a Z' produced in association with b-jets. Therefore, the obtained exclusion limits on the Z' mass are lower than the mass-exclusion limits of the inclusive analysis.

With the logarithmic binning used by the inclusive analysis applied, the limits obtained in this analysis become closer to the limits set by the inclusive search but are still lower by roughly 500 GeV in the electron channel and 200 GeV in the muon channel. The inclusive analysis considers systematic uncertainties which are currently not considered in this analysis. Therefore, the difference between the obtained limits is expected to increase further when systematic uncertainties are also considered in this analysis. The low event statistics in the high dilepton invariant mass region additionally make it necessary to use a different

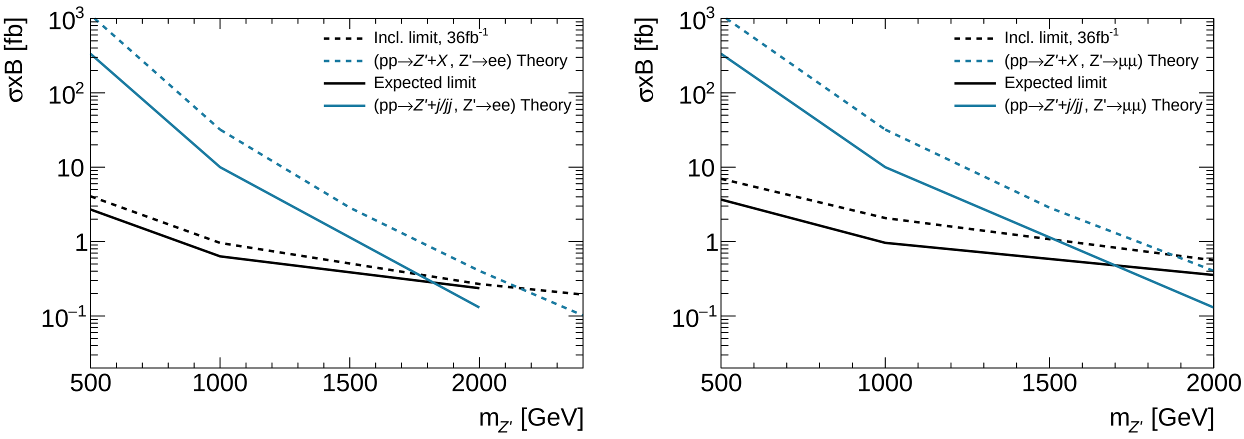

Figure 8.5.: Comparison of the Z' mass exclusion limit obtained in this analysis with the logarithmic binning in the $\sigma(E_{\mathrm{T}}^{\mathrm{miss}})$ signal region and the limit obtained in the inclusive analysis [50] for the electron channel (left) and muon channel (right).

method for the limit setting, such as a limit calculation using a toy dataset created by MC algorithms.

It also has to be noted that searches for Z' models with specific couplings can be of interest independently of the inclusive searches. A recent search for a Z' that couples to third-generation quarks only and decays exclusively to $b\bar{b}$ excluded the mass range between 1.3 TeV and 1.45 TeV at 95% CL [52].

9. Conclusion and Outlook

A search for a Z' boson produced in association with b-jets is presented in this thesis. A preliminary expected exclusion limit on the Z' mass is set in order to estimate the sensitivity of the chosen analysis approach. The analysis is carried out using the data collected by the ATLAS detector at a centre-of-mass energy $\sqrt{s} = 13\,\text{TeV}$ in 2015 and 2016, corresponding to an integrated luminosity of $36.2\,\text{fb}^{-1}$.

The final state of the considered signal processes for a Z' production is characterized by the presence of two leptons of the same flavour and at least one b-jet. Based on this signature, a preselection region is defined for both leptonic decay channels of the Z' considered in the analysis, referred to as electron channel and muon channel respectively. The contribution of background events originating from SM processes to the preselection region is estimated from MC simulations and the Matrix Method, a data-driven method for estimating the so-called multijet background originating from events with jets being misidentified as leptons by the detector. The multijet background is considered for the electron channel only. For both channels, the largest source of background events are dileptonic $t\bar{t}$ decays. The modelling of the $t\bar{t}$ background is studied in a comparison between data and MC in a dedicated control region, reaching the conclusion that the $t\bar{t}$ background is well modelled. The agreement between data and all considered background processes is studied in another dedicated validation region and also found to be good.

For both lepton channels, Z' signal samples are studied for Z' masses of 0.5 TeV, 1 TeV and 2 TeV. Two different approaches for a final event selection are explored, one with a requirement on $\sigma(E_{\mathrm{T}}^{\mathrm{miss}})$ and one with an event selection optimized per NN. For both signal regions, exclusion limits on the Z' mass are set. The binning of the dilepton invariant mass distributions used in the signal regions for the limit extraction is determined from the detector resolution of the dilepton invariant mass. A limit of 1.6 TeV is obtained for both signal regions and both lepton channels.

The limit is compared to the result of a previous analysis, which used the 2015/16 dataset and considered an inclusive Z' production cross section. The Z' model considered in the inclusive analysis differs from the model considered in this analysis, as it allows for couplings between the Z' and quarks of the first generation. Limits of 1.9 TeV for the muon channel and 2.2 TeV for the electron channel were obtained in the inclusive analysis.

The binning of the dilepton invariant mass distribution used in the inclusive analysis is applied to the signal regions in order to study the impact on the obtained limits. With this approach, better limits of 1.7 TeV for the muon channel and 1.8 TeV for the electron channel are obtained, nevertheless staying below the limits obtained in the inclusive search. However, the comparison is not straightforward due to the different Z' models, and searches for a Z' with specific couplings are still of interest, such as the recent search for a Z' exclusively coupling to third-generation quarks which excluded a mass region between 1.3 TeV and 1.45 TeV.

Several steps can be taken to proceed with the analysis. As the framework used for the limit setting is not specialised in resonant searches, a different framework should be tried in order to study the impact on the obtained limit. Additional signal samples for different Z' masses would allow for a more precise determination of the exclusion limit, which is currently determined from an extrapolation using three mass points only. The usage of the full Run 2 dataset would additionally increase the event statistics, improving the statistical uncertainties considerably which is especially important in the high invariant mass region where very few signal and background events are expected. For a complete analysis, systematic uncertainties have to be considered as well as an uncertainty on the multijet background estimation, whereas the analysis presented in this thesis considered statistical uncertainties of the MC samples only.

A. Appendix

A.1. Fake Efficiencies

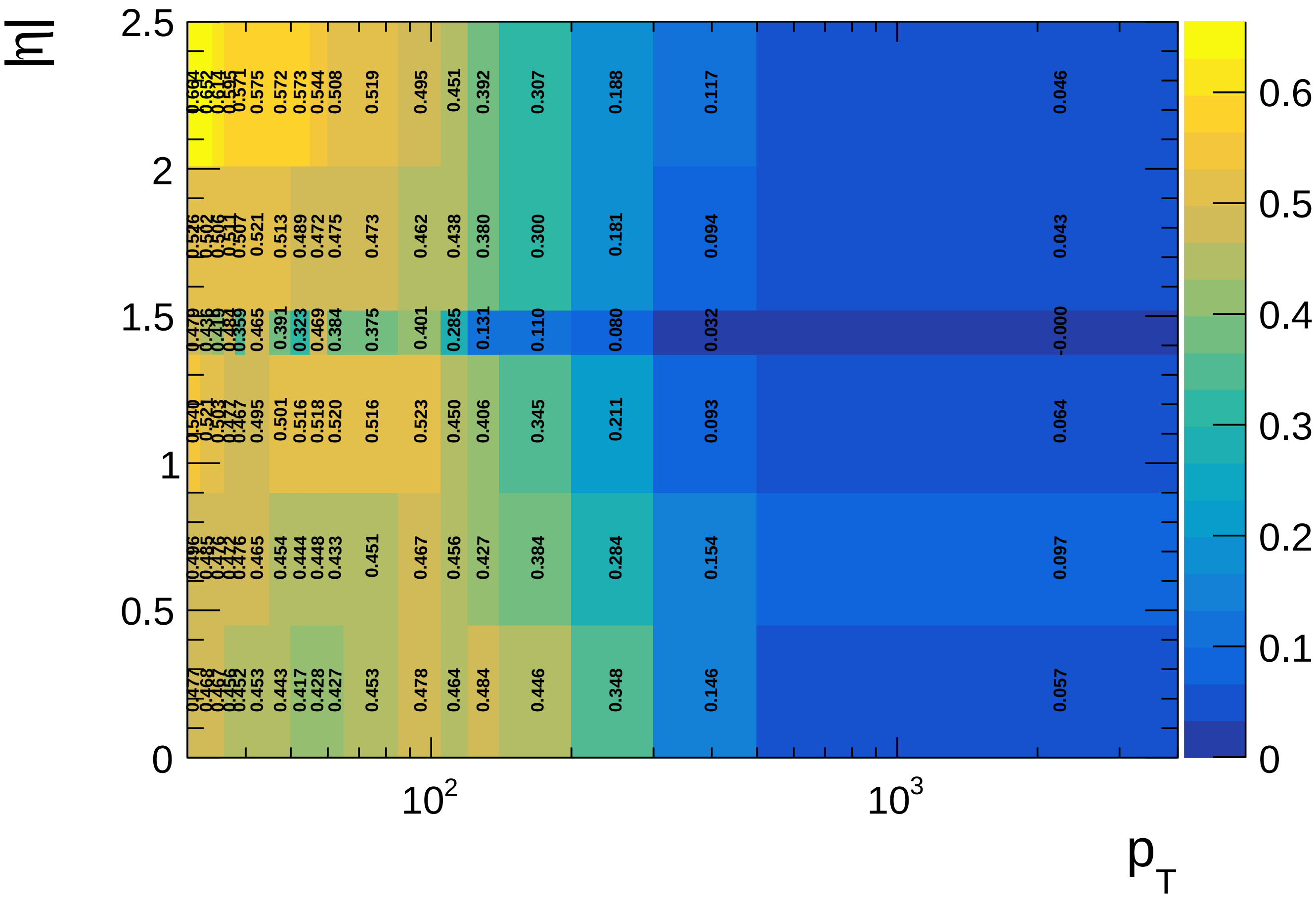

Figure A.1.: Fake efficiencies used for this analysis binned in p_{T} and $|\eta|$. The efficiencies were calculated for a SM analysis of Drell-Yan processes in the high dilepton invariant mass region by Ricardo González López (University of Liverpool).

A.2. Background Validation

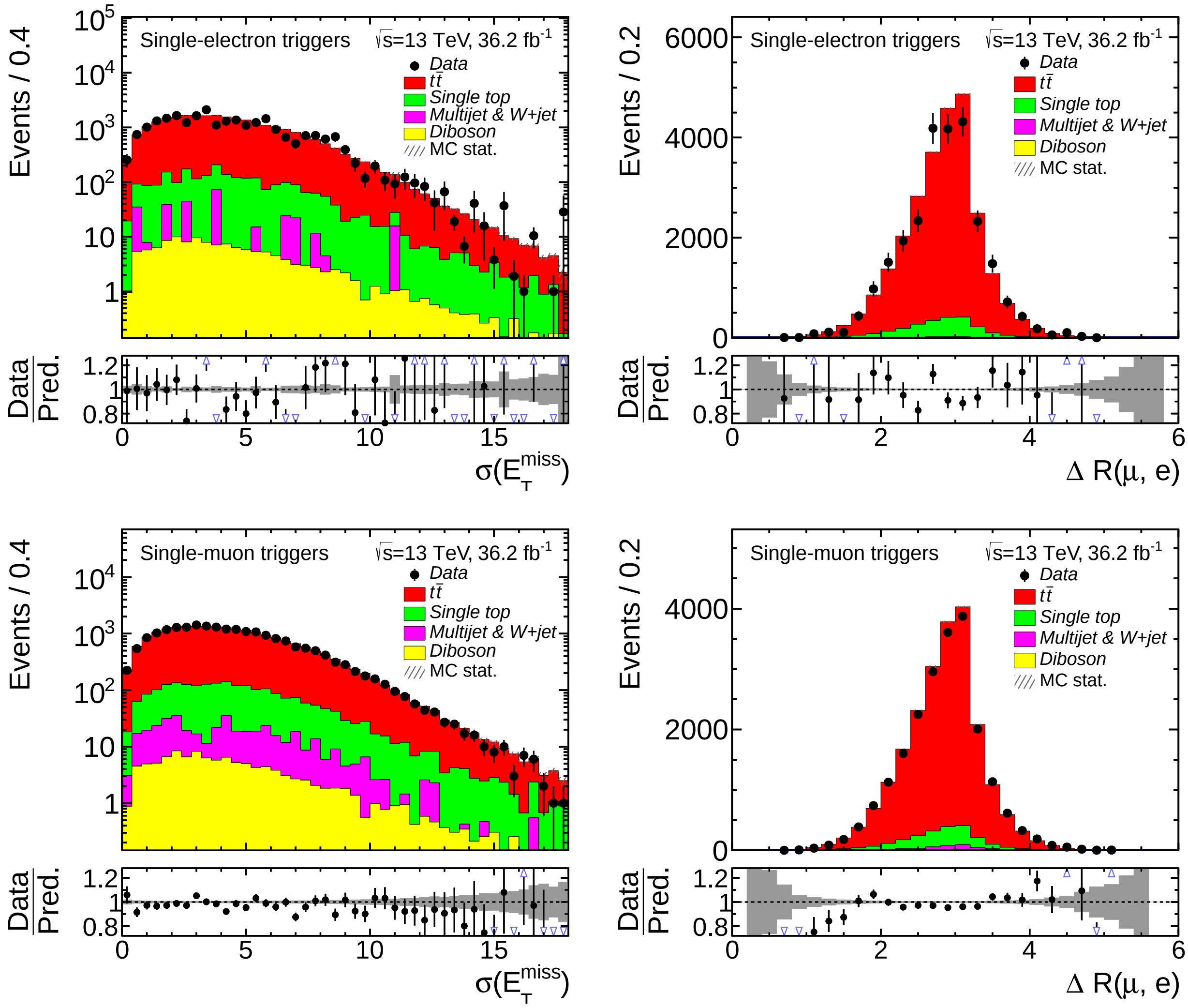

Figure A.2.: $\sigma(E_{\mathrm{T}}^{\mathrm{miss}})$ and $\Delta R(e\mu)$ obtained with single-electron and single-muon triggers.

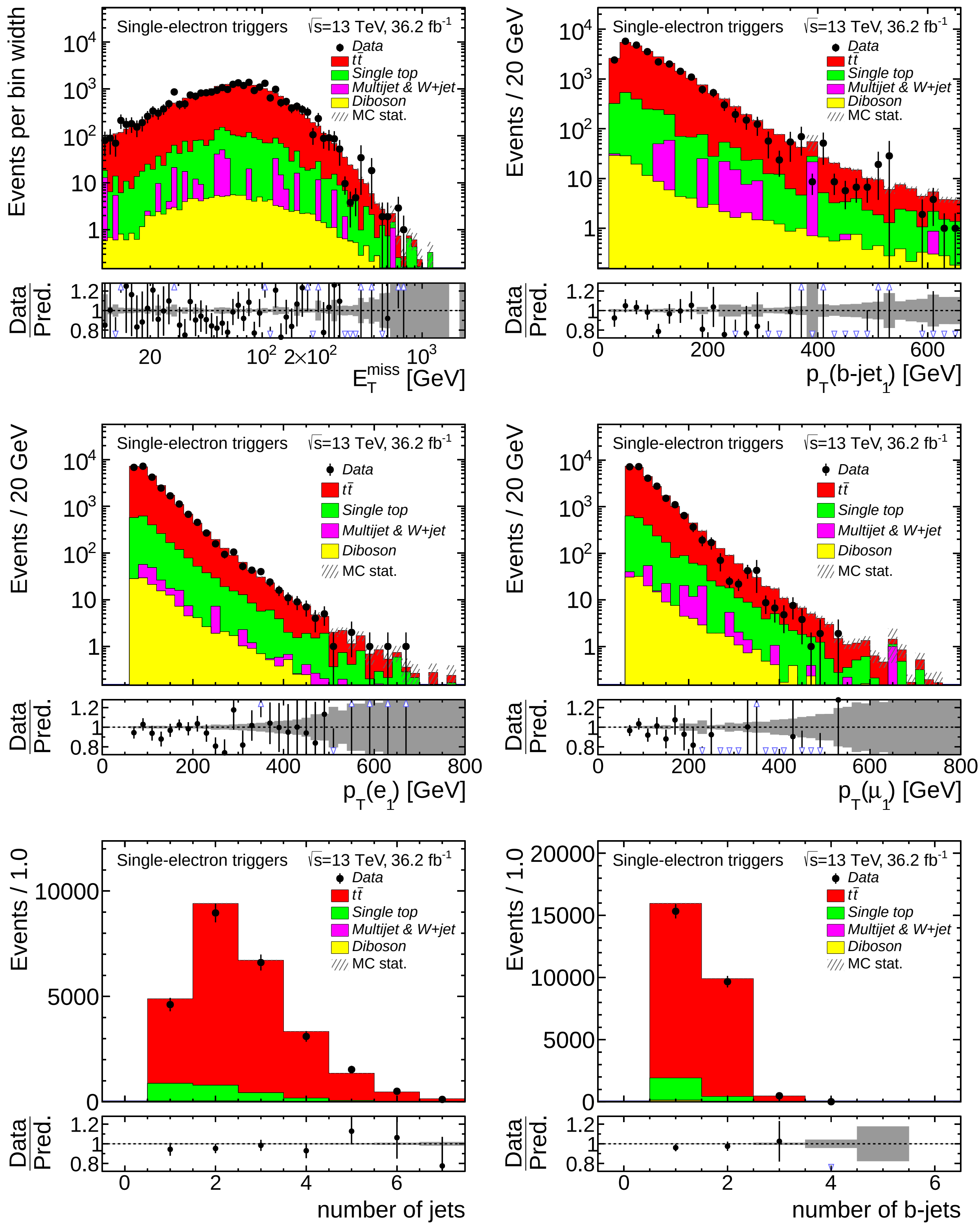

Figure A.3.: $E_{\mathrm{T}}^{\mathrm{miss}}$, p_{T} of the leptons and of the p_{T}-leading b-jet, jet multiplicity and b-jet multiplicity obtained with single-electron triggers.

Table A.1.: Single-electron triggers with the respective prescale factors and p_{T} range of the electron for which the respective trigger is applied.

Year	Trigger	Average prescale factor	p_{T} range [GeV]
2016	e26_lhvloose_nod0_L1EM20VH	110.02	$30-65$
	e60_lhvloose_nod0	28.50	$65-126$
	e120_lhvloose_nod0	15.27	$126-147$
	e140_lhvloose_nod0	1.90	$147-315$
	e300_etcut	1.0	>315
2015	e26_lhvloose_nod0_L1EM20VH	125.0	$30-65$
	e60_lhvloose_nod0	12.0	$65-315$
	e200_etcut	1.0	>315

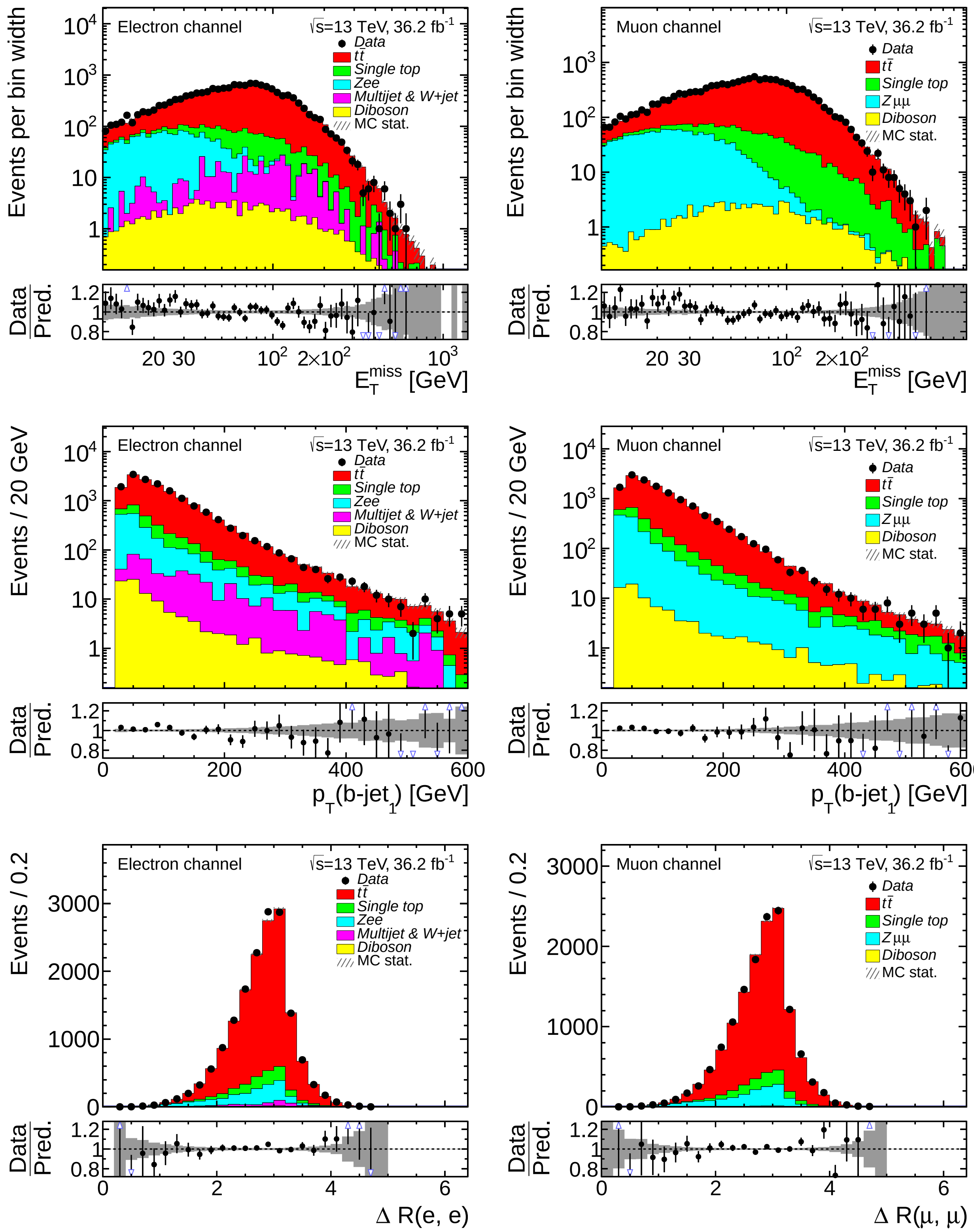

Figure A.4.: $E_{\mathrm{T}}^{\mathrm{miss}}$, p_{T} of the p_{T}-leading b-jet and $\Delta R(\ell\ell)$ of the combined background validation region for the electron channel (left) and muon channel (right).

A.3. Signal Samples

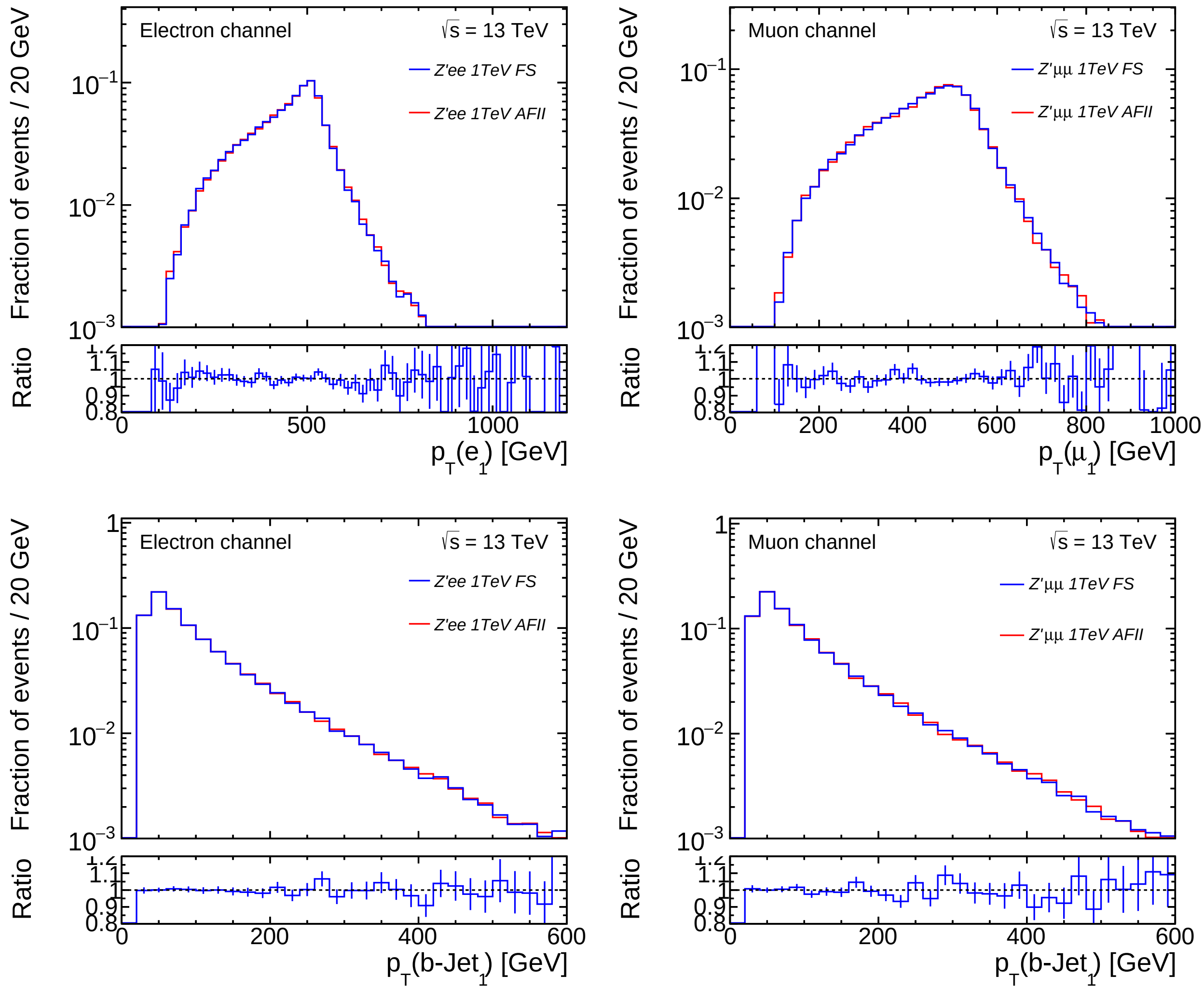

Figure A.5.: p_{T} distributions for the p_{T}-leading lepton and p_{T}-leading b-jet obtained with FullSim and Atlfast II samples of the electron channel (left) and muon channel (right).

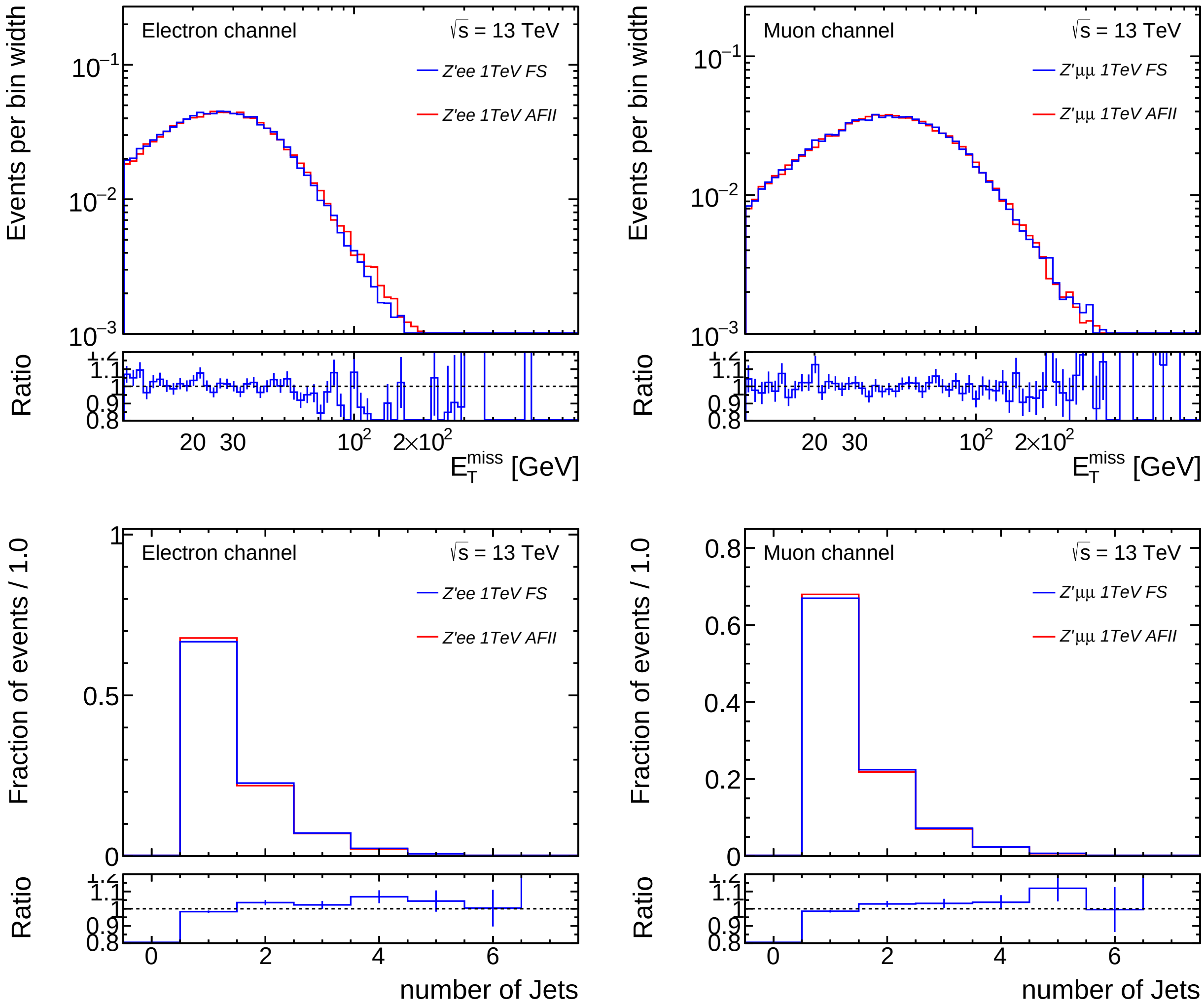

Figure A.6.: $E_{\mathrm{T}}^{\mathrm{miss}}$ distribution and jet multiplicity obtained with FullSim and Atlfast II samples of the electron channel (left) and muon channel (right).

Table A.2.: Signal samples cutflow for the elecron channel.

Selection criterion	Z'ee 0.5 TeV	Z'ee 1 TeV	Z'ee 2 TeV
two signal electrons	144292	149610	160830
no signal muons	144237	149533	160765
at least one b-tagged jet	92166	95567	101013
passed dielectron trigger	89535	93224	98914
jet cleaning	89319	92982	98670
electron $p_{\mathrm{T}} > 65$ GeV	86726	92721	98581
$\mathrm{M}_{ee} > 130$ GeV	86724	92714	98573
$1.37 < \lvert\eta_{\mathrm{cl}}^{e_1}\rvert < 1.52$	82834	88820	94665
$1.37 < \lvert\eta_{\mathrm{cl}}^{e_2}\rvert < 1.52$	78504	84213	90081

Table A.3.: Signal samples cutflow for the muon channel.

Selection criterion	Z'$\mu\mu$ 0.5 TeV	Z'$\mu\mu$ 1 TeV	Z'$\mu\mu$ 2 TeV
no signal electrons	199499	192979	198009
two signal muons	107537	106766	109261
at least one b-tagged jet	75543	73063	72384
passed single-muon trigger	73742	71299	70528
jet cleaning	73573	71117	70342
bad muon veto	73499	70039	67370
muon $p_{\mathrm{T}} > 65$ GeV	70116	69534	67217
$\mathrm{M}_{\mu\mu} > 130$ GeV	70112	69532	67217

Table A.4.: Event yields of background and signal events in the preselection region (presel.) and with and additional event selection requirement of $\sigma(E_{\mathrm{T}}^{\mathrm{miss}}) < 4.0$.

Signal sample	Background		Signal		Sover B	%
	presel.	$\sigma(E_{\mathrm{T}}^{\mathrm{miss}}) < 4.0$	presel.	$\sigma(E_{\mathrm{T}}^{\mathrm{miss}}) < 4.0$	presel.	$\sigma(E_{\mathrm{T}}^{\mathrm{miss}}) < 4.0$
Z'ee 0.5 TeV	16180	8717	3634	3410	22.46	39.12
Z'ee 1 TeV	16180	8717	119	110	0.74	1.26
Z'ee 2 TeV	16180	8717	1.6	1.46	0.01	0.017
Z'$\mu\mu$ 0.5 TeV	13770	7474	2830	2654	20.5	35.6
Z'$\mu\mu$ 1 TeV	13770	7474	88	82	0.64	1.1
Z'$\mu\mu$ 2 TeV	13770	7474	1.1	1.04	0.008	0.014

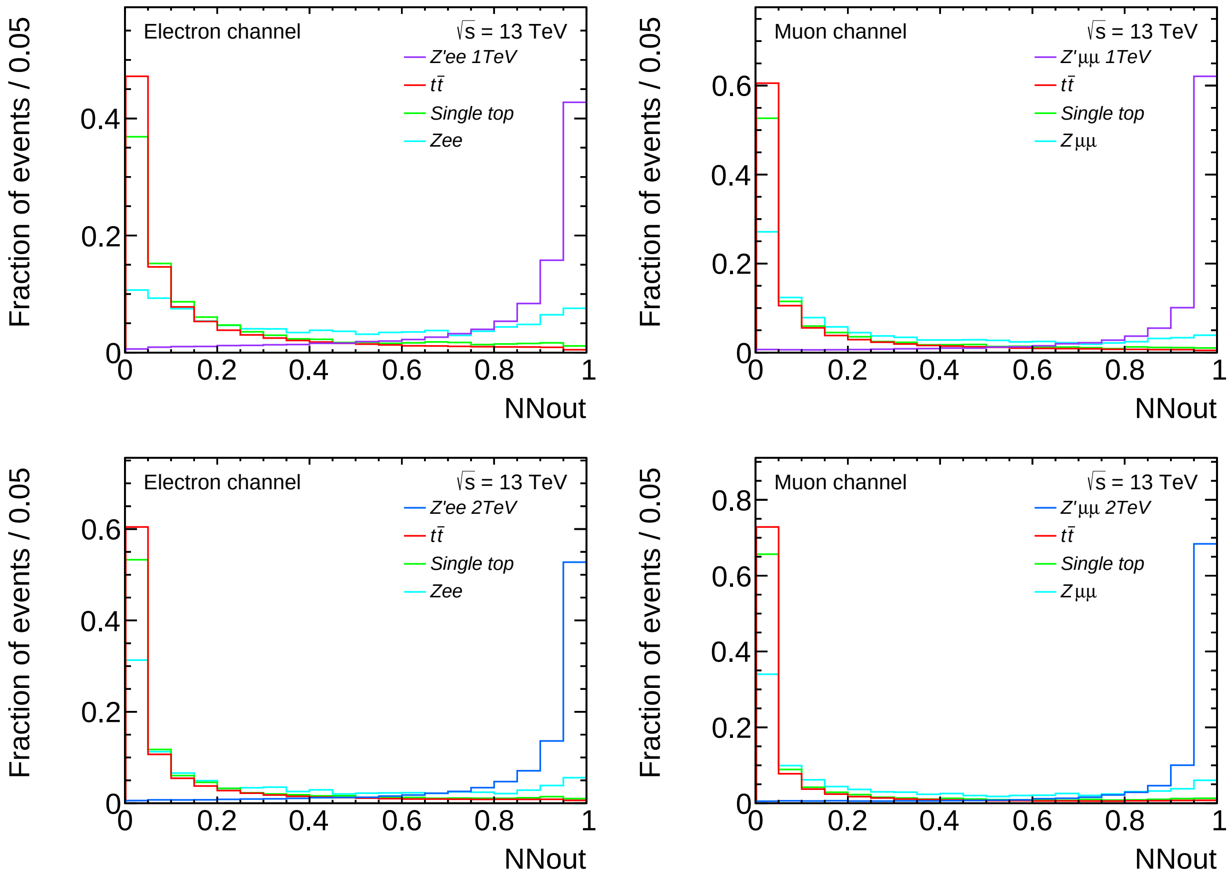

Figure A.7.: NNout distribution obtained for the Z'$\ell\ell$ signal samples with Z' masses of 1 TeV and 2 TeV for the electron channel (left) and for the muon channel (right).

A.4. Exclusion Limits

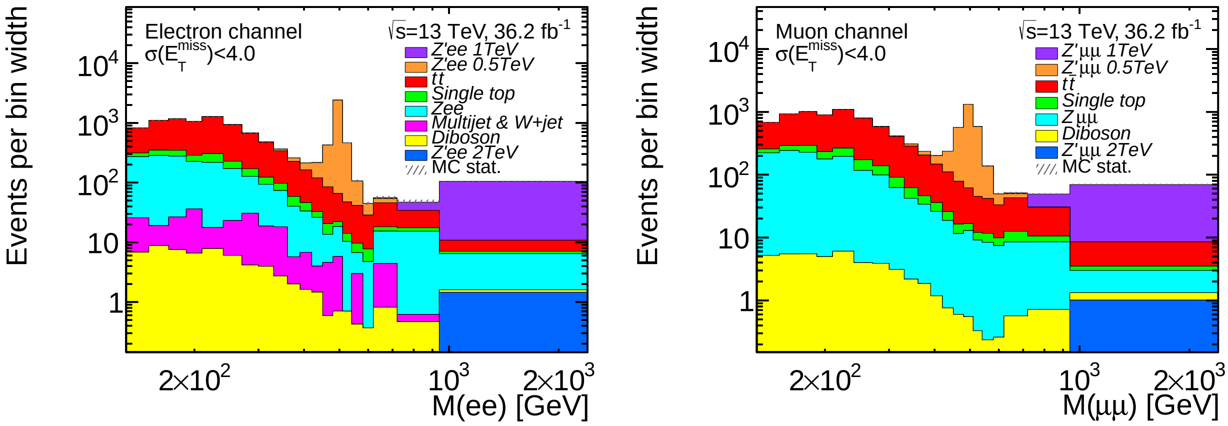

Figure A.8.: Dielepton invariant mass spectra obtained with $\sigma(E_{\mathrm{T}}^{\mathrm{miss}}) < 4.0$ and the binning chosen for the limit setting for the electron channel (left) and muon channel (right).

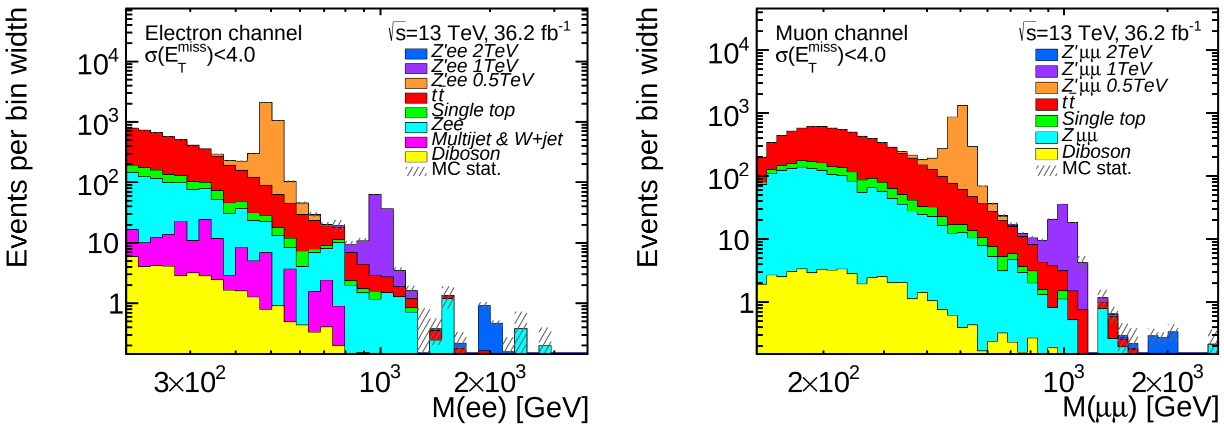

Figure A.9.: Dielepton invariant mass spectra obtained with $\sigma(E_{\mathrm{T}}^{\mathrm{miss}}) < 4.0$ and a logarithmic binning for the electron channel (left) and muon channel (right).

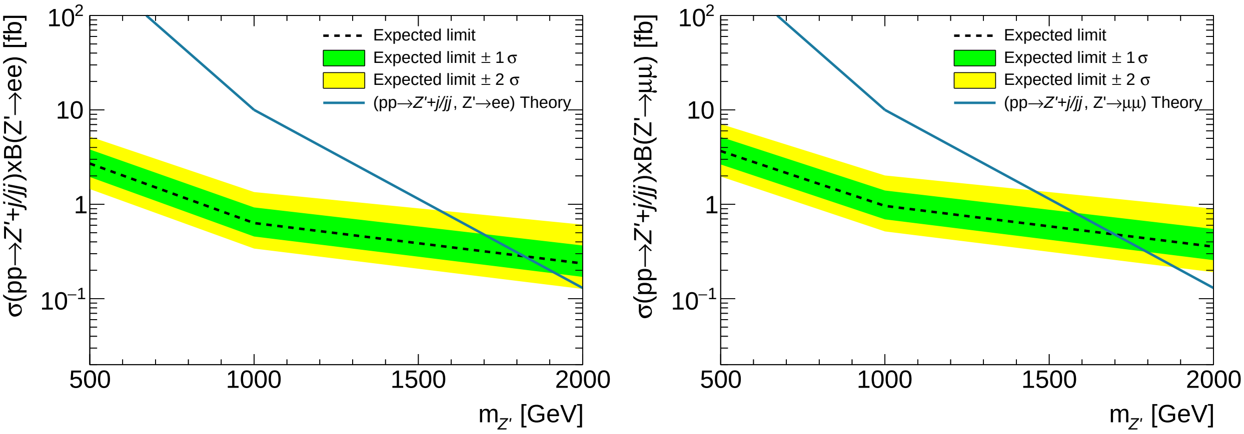

Figure A.10.: Expected 95% CL upper limit on the cross section for the Z' production obtained with a logarithmic binning in the signal region with a signal selection per $\sigma(E_{\mathrm{T}}^{\mathrm{miss}}) < 4.0$ for the electron channel (left) and the muon channel (right).

List of Figures

List of Tables

Bibliography

[1] D. Griffiths, *Introduction to elementary particles.* Wiley-VCH, 2008.

[2] ATLAS Collaboration, *Observation of a new particle in the search for the Standard Model Higgs boson with the ATLAS detector at the LHC*, Phys. Lett. B **716** (2012) 1, `arXiv:1207.7214 [hep-ex]`.

[3] CMS Collaboration, *Observation of a new boson at a mass of 125 GeV with the CMS experiment at the LHC*, Phys. Lett. B **716** (2012) 30, `arXiv:1207.7235 [hep-ex]`.

[4] `https://commons.wikimedia.org/w/index.php?curid=4286964`.
last accessed October 20th, 2021.

[5] P. A. Zyla et al. (Particle Data Group), *Review of Particle Physics*, Prog. Theor. Exp. Phys. **2020** (2020) 261.

[6] W. Altmannshofer, S. Gori, M. Pospelov, and I. Yavin, *Quark flavor transitions in* $L_\mu - L_\tau$ *models*, Phys. Rev. D **89** (2014) 095033, `arXiv:1403.1269 [hep-ph]`.

[7] L. Maiani, *The GIM Mechanism: origin, predictions and recent uses*, 2013, `arXiv:1303.6154 [hep-ph]`.

[8] LHCb Collaboration, *Test of lepton universality in beauty-quark decays*, 2021, `arXiv:2103.11769 [hep-ex]`.

[9] LHCb Collaboration, *Measurement of CP Averaged Observables in the* $B \to K^*\mu^+\mu^-$ *Decay*, Phys. Rev. Lett. **125** (2020) 011802, `arXiv:2003.04831 [hep-ex]`.

[10] S. Descotes-Genon, J. Matias, M. Ramon, and J. Virto, *Implications from clean observables for the binned analysis of* $B \to K^*\mu^+\mu^-$ *at large recoil*, JHEP **2013** (2013), `arXiv:1207.2753 [hep-ph]`.

[11] M. Algueró et al., *Emerging patterns of New Physics with and without Lepton Flavour Universal contributions*, Eur. Phys. J C **79** (2019), `arXiv:1903.09578 [hep-ph]`.

[12] J. M. Campbell, J. W. Huston, and W. J. Stirling, *Hard interactions of quarks and gluons: a primer for LHC physics*, Rep. Prog. Phys. **70** (2006) 89, `arXiv:hep-ph/0611148 [hep-ph]`.

[13] R. D. Ball et al., *Parton distributions for the LHC run II*, JHEP **2015** (2015), `arXiv:1410.8849 [hep-ph]`.

[14] M Tabanashi et al., *Review of Particle Physics*, Phys. Rev. D **98** (2018) 030001.

[15] L. Evans and P. Bryant, *LHC Machine*, JINST **3** (2008) S08001.

[16] J. Haffner, *The CERN accelerator complex. Complexe des accélérateurs du CERN*, http://cds.cern.ch/record/1621894, General Photo.

[17] ATLAS Collaboration, *The ATLAS Experiment at the CERN Large Hadron Collider*, JINST **3** (2008) S08003.

[18] CMS Collaboration, *The CMS experiment at the CERN LHC*, JINST **3** (2008) S08004.

[19] LHCb Collaboration, *The LHCb Detector at the LHC*, JINST **3** (2008) S08005.

[20] ALICE Collaboration, *The ALICE experiment at the CERN LHC*, JINST **3** (2008) S08002.

[21] https://lhc-commissioning.web.cern.ch/schedule/LHC-long-term.htm? last accessed September 1st, 2021.

[22] W. Herr and B. Muratori, *Concept of luminosity*, CAS (2006) 361, https://cds.cern.ch/record/941318.

[23] https://twiki.cern.ch/twiki/bin/view/AtlasPublic/LuminosityPublicResultsRun2, last accessed August 13th, 2021.

[24] ATLAS IBL Collaboration, *Production and Integration of the ATLAS Insertable B-Layer*, JINST **13** (2018) T05008, arXiv:1803.00844v3 [physics.ins-det].

[25] ATLAS Collaboration, *Performance of the ATLAS trigger system in 2015*, Eur. Phys. J C **77** (2017), arXiv:1803.00844 [physics.ins-det].

[26] S. Alioli, P. Nason, C. Oleari, and E. Re, *A general framework for implementing NLO calculations in shower Monte Carlo programs: the POWHEG BOX*, JHEP **2010** (2010), arXiv:1002.2581 [hep-ph].

[27] T. Sjöstrand, et al, *An introduction to PYTHIA 8.2*, Comput. Phys. Commun. **191** (2015) 159, arXiv:1410.3012 [hep-ph].

[28] D. J. Lange, *The EvtGen particle decay simulation package*, Nucl. Instrum. Meth. **462** (2001) 152.

[29] T. Gleisberg et al., *Event generation with SHERPA 1.1*, JHEP **2009** (2009) 007, arXiv:0811.4622 [hep-ph].

[30] S. Agostinelli et al., *Geant4—a simulation toolkit*, Nucl. Instrum. Meth. **506** (2003) 250.

[31] J. Alwall et al., *The automated computation of tree-level and next-to-leading order differential cross sections, and their matching to parton shower simulations*, JHEP **2014** (2014), arXiv:1405.0301 [hep-ph].

[32] L. Lönnblad and S. Prestel, *Matching tree-level matrix elements with interleaved showers*, JHEP **2012** (2012), `arXiv:1109.4829 [hep-ph]`.

[33] W. Lukas, *Fast Simulation for ATLAS: Atlfast-II and ISF*, tech. rep., 2012.

[34] ATLAS Collaboration, *Electron reconstruction and identification in the ATLAS experiment using the 2015 and 2016 LHC proton–proton collision data at $\sqrt{s} = 13$ TeV*, Eur. Phys. J C **79** (2019), `arXiv:1902.04655v2 [physics.ins-det]`.

[35] ATLAS Collaboration, *Muon reconstruction performance of the ATLAS detector in proton–proton collision data at $\sqrt{s} = 13$TeV*, Eur. Phys. J C **76** (2016), `arXiv:1603.05598v2 [hep-ex]`.

[36] ATLAS Collaboration, *Jet reconstruction and performance using particle flow with the ATLAS Detector*, Eur. Phys. J C **77** (2017), `arXiv:1703.10485v2 [hep-ex]`.

[37] M. Cacciari, G. P. Salam, and G. Soyez, *The anti-ktjet clustering algorithm*, JHEP **2008** (2008) 063, `arXiv:0802.1189v2 [hep-ph]`.

[38] ATLAS Collaboration, *ATLAS b-jet identification performance and efficiency measurement with $t\bar{t}$ events in pp collisions at $\sqrt{s} = 13$TeV*, Eur. Phys. J C **79** (2019), `arXiv:1907.05120v2 [hep-ex]`.

[39] ATLAS Collaboration, *Expected performance of missing transverse momentum reconstruction for the ATLAS detector at $\sqrt{s} = 13$TeV*, 2015, `https://cds.cern.ch/record/2037700`.

[40] ATLAS Collaboration, *Selection of jets produced in 13TeV proton-proton collisions with the ATLAS detector*, `https://cds.cern.ch/record/2037702`.

[41] ATLAS Collaboration, *Measurement of the double-differential high-mass Drell-Yan cross section in pp collisions at $\sqrt{s} = 8$ TeV with the ATLAS detector*, JHEP **2016** (2016), `arXiv:1606.01736 [hep-ex]`.

[42] L. Sommer, *Untersuchungen zur Kinematik von schweren Zwei-Lepton Resonanzen mit assoziierten b-Quarks im Vergleich zum Untergrund*, 2021. Bachelor Thesis, Bergische Universität Wuppertal.

[43] M. T. Hagan, H. B. Demuth, M. H. Beale, and O. D. Jesús, *Neural network design.* 2 ed., 2014.

[44] M. Feindt and U. Kerzel, *The NeuroBayes neural network package*, Nucl. Inst. Meth. **559** (2006) 190.

[45] M. Feindt, *A Neural Bayesian Estimator for Conditional Probability Densities*, 2004, `arXiv:physics/0402093v1 [physics.data-an]`.

[46] A. L. Read, *Presentation of search results: the CL_s technique*, J. Phys. G **28** (2002) 2693.

[47] W. Verkerke and D. Kirkby, *The RooFit toolkit for data modeling*, CHEPP03 (2003), arXiv:physics/0306116v1 [physics.data-an].

[48] G. Cowan, K. Cranmer, E. Gross, and O. Vitells, *Asymptotic formulae for likelihood-based tests of new physics*, Eur. Phys. J C **71** (2011), arXiv:1007.1727 [physics.data-an].

[49] S. Wilks, *The large-sample distribution of the likelihood ratio for testing composite hypotheses*, Ann. Math. Statist. (1938) 60.

[50] ATLAS Collaboration, *Search for new high-mass phenomena in the dilepton final state using 36 fb^{-1} of proton-proton collision data at $\sqrt{s} = 13$ TeV with the ATLAS detector*, JHEP **10** (2017), arXiv:1707.02424 [hep-ex].

[51] ATLAS Collaboration, *Search for high-mass dilepton resonances using 139 fb^{-1} of pp collision data collected at s=13 TeV with the ATLAS detector*, Phys. Lett. B **796** (2019) 68, arXiv:1903.06248 [hep-ex].

[52] ATLAS Collaboration, *Search for heavy particles in the b-tagged dijet mass distribution with additional b-tagged jets in proton-proton collisions at $\sqrt{s} = 13$ TeV with the ATLAS experiment*, 2021, arXiv:2108.09059 [hep-ex].